Geomechanics for Energy and the Environment 17 (2019) 29–46

Contents lists available at ScienceDirect

Geomechanics for Energy and the Environment

journal homepage: www.elsevier.com/locate/gete

3D modelling of the Excavation Damaged Zone using a Marked Point Process technique

Andrés Alcolea Rodríguez [a,*], Uli Kuhlmann [b], Paul Marschall [c]

[a] HydroGeoModels AG, Tösstalstrasse 23, 8400 Winterthur, Switzerland
[b] TK Consult AG, Mainaustrasse 30, 8008 Zürich, Switzerland
[c] Nagra (Nationale Genossenschaft für die Lagerung radioaktiver Abfälle), Hardstrasse 73, 5430 Wettingen, Switzerland

HIGHLIGHTS

- An efficient approach for the 3D stochastic modelling of the Excavation Damaged Zone is proposed.
- The approach relies on 2D geomechanical simulations as training data sets.
- Two applications, including the calibration of a complex hydraulic test in Mont Terri (Switzerland), are presented.

ARTICLE INFO

Article history:
Received 19 December 2017
Received in revised form 6 April 2018
Accepted 15 July 2018
Available online 24 July 2018

Keywords:
Excavation Damage Zone
3D stochastic modelling
Marked Point Process
Deep geological repository
Radioactive waste

ABSTRACT

The Excavation Damage Zone (EDZ) is a key aspect in the assessment of engineering feasibility and long-term safety of deep geological repositories for radioactive waste. The EDZ represents a possible release path for radionuclides dissolved in the porewater and for gases from corrosion and degradation processes which needs to be addressed quantitatively in Safety Assessment (SA). The EDZ is often represented by a discrete fracture network, whose complexity precludes its implementation in conventional SA models. To overcome this problem, two-dimensional abstraction methodologies have been developed that replace the complex geometry of the discrete fracture network by a hydraulically equivalent continuum model. Although such simple 2D models are amenable to SA modelling, they cannot capture the inherent three-dimensional and stochastic nature of the phenomena associated with the EDZ. In this paper we present a methodology based on Marked Point Processes to infer 3D stochastic continuum models of the EDZ from 2D discrete characterizations of the fracture network. The methodology is illustrated with the calibration of a multi-rate injection experiment in Mont Terri (Switzerland).

1. Introduction

Deep geological repositories are widely accepted as possibly the best solution for radioactive waste disposal and confinement. Isolation is achieved by a combination of engineered (e.g., bentonite) and natural barriers (e.g., indurated clays). Current plans envisage a mined repository comprising tunnels or caverns, into which packaged waste is placed. The excavation and emplacement processes lead to the so-called repository-induced effects.[1] Amongst them we highlight the Excavation Damage Zone (EDZ) around galleries and shafts of the repository, because it represents a viable release path for radionuclides and corrosion and degradation gases. Thus, it is not strange that a large volume of research is being devoted to this topic.[2–4]

In indurated clays and, in general, in low permeability media, fluid flow and gas transport are predominant through discrete discontinuities, either natural or induced by the excavation process. Thus, Discrete Fracture Network (DFN) models are ideally suited to represent the associated thermo-hydro-chemo-mechanical phenomena. However, DFN models are complex and CPU costly (and therefore deterministic) representations of the EDZ that are not amenable to long-term Probabilistic Safety Assessment (PSA) of the deep geological repositories.[5,6] To overcome this computational problem, upscaling and abstraction methods[7,8] have been developed to reduce the complexity of the DFN models while retaining the main features of their behaviour. Jackson et al.[5] suggest the use of continuum porous medium (CPM) models that are computationally practicable in the context of Performance Assessment. Lanyon & Senger[9] compare three different models using generic (although realistic) data representative of the Opalinus Clay in Switzerland, i.e., a DFN, an equivalent CPM upscaled from it, and a simplified shell-like CPM suitable for use within PSA. A similar approach

* Corresponding author.
E-mail addresses: andres.alcolea@hydrogeomodels.ch (A. Alcolea Rodríguez), kuhlmann@tkconsult.ch (U. Kuhlmann), Paul.Marschall@nagra.ch (P. Marschall).

https://doi.org/10.1016/j.gete.2018.07.003
2352-3808/

is presented for the modelling of a repository in the Callovo-Oxfordian clay.[10,11] Alcolea et al.[6] present a heuristic approach to represent the creation and evolution of the EDZ in an abstracted and simplified manner. The key features of the approach are the stochastic character of the excavation-induced fracture network and the self-sealing processes associated with the re-saturation after backfilling of the galleries. The approach is applied (1) to a range of generic repository settings to investigate the hydraulic significance of the EDZ after repository closure, and (2) to the modelling of a self-sealing experiment at the Mont Terri Underground Rock Laboratory (URL) in Switzerland.

Existing approaches aimed at simplifying the geometry of the EDZ suffer from two main drawbacks arising from the high CPU and RAM consumption of the DFN simulators. First, DFN models are most often the result of two-dimensional geomechanical simulations that represent a cross-section orthogonal to the gallery/shaft axis and assume plane stress. Correspondingly, the connectivity of the EDZ and relevant migration paths parallel to the gallery are disregarded. Second, the number of DFN realizations (and corresponding one-to-one abstracted EDZ models) mimicking given in-situ stress state and rock strength conditions, is very limited. The CPU problem is being tackled nowadays by implementing more efficient numerical methods (which are, in essence, very similar; see a complete review in Ref. 12) like bonded particle modelling,[13–15] modified Voronoi tessellation methods,[16] discrete element methods[17] or hybrid methods.[18] Besides computational effort, other issues associated with DFN simulators are related to parameter uncertainty and oversimplifying physical assumptions (with corresponding formulations) not yet validated.[19]

Regardless of the numerical method, the rapid rendering of complex 3D simulations of the EDZ still remains a challenge due to the extreme level of refinement of both spatial and temporal model discretizations required to mimic the excavation process. Until this problem is overcome, an ideal abstraction method should render (in a reasonable amount of time) many 3D continua heterogeneous (or piece-wise heterogeneous in the case of shell-like abstracted models) EDZ simulations that inherit the geometric features of a limited number of discrete fracture networks. This problem can be cast in the framework of multiple-point geostatistical techniques (see reviews in Refs. 20,21). Unlike traditional geostatistics, multiple-point methods avoid the explicit definition of a random function (e.g., a variogram or a covariance function) to model heterogeneity, but directly infer the necessary multivariate distributions from so-called "training images" (TI) that represent a conceptual model of what is being modelled. Training images can be either categorical[22] or continuum.[23] Simulations inherit (but are not conditioned to) the geometric patterns, defined as spatial arrangements of values, and high-order statistics (e.g., histograms of the properties) of the TI (or TIs). Indeed, simulations can be conditioned to hard data if available and to secondary variables.[24] Comunian et al.[25] efficiently solve the problem of rendering 3D simulations out of two (or more) TIs defined along orthogonal cartesian planes. In our case, DFNs are coherent with the in-situ stress state, rock parameters, etc. and represent a conceptual "binary" model (i.e., 0 for matrix, 1 for fracture) of the extent and geometry of the EDZ. Correspondingly, the upscaled CPM represents a continuum conceptual model of the hydraulic properties of the EDZ. As such, both DFN and CPM are good candidates as training image. However, although multiple-point geostatistical techniques are appealing, its use in this context is not straightforward and the associated CPU consumption is very high.

An alternative to overcome the limitations of multiple-point geostatistical techniques is the so-called Marked Point Process (MPP). In geostatistics, a point process is a random process represented by a set of isolated points that represent objects (e.g., a fracture represented by its centroid). Each point is attributed with random variables, termed "marks", that describe the associated object and its properties (e.g., fracture extent and Euler angles, roughness, etc.) by means of probability density functions (pdf). This method, originally formulated in the context of percolation theory (see a review in Ref. 26), has gained popularity during recent years, up to the point of becoming a standard for image processing.[27] In the framework of stochastic discrete fracture modelling, Xu & Dowd[28] presented the commercial software FracSim3D, based on MPP techniques. The software generates 2D and 3D DFNs from pdfs inferred from composites of 2D and 3D training data sets. Training data sets are generally the outcomes of scanlines, rock outcrops, core samples, geophysical logging, etc. The code has undergone several upgrades and modifications.[29–31] In this work, we have adapted the method of Xu & Dowd[28] to (1) acquire the pdfs representing fracture properties directly from a DFN and, (2) generate 3D discrete fracture networks directly from 2D training images. The code has been parallelized, what allows rendering a large number of simulations using low CPU and RAM resources. In addition, a new method for consistent sampling of fracture properties has been implemented and some consistency checks of the intersections between generated fractures have been introduced.

This paper is organized as follows. First, the methodology is outlined and illustrated using a realistic DFN corresponding to the gallery of a hypothetic high-level waste geological repository. Second, the methodology is applied to the calibration of a multi-rate injection experiment in the Mont Terri Underground Rock Laboratory (Switzerland). The paper ends with some conclusions about the use of Marked Point Process techniques in the 3D modelling of the Excavation Damage Zone.

2. Methodology

The objective is to generate many 3D stochastic continuum porous media models out of a limited number of 2D fracture networks, used as training images. The training image is obtained by hydromechanical modelling and mimics a possible geometry of the EDZ after excavation. The 3D simulations must therefore inherit the physics of the process, as represented by the geometric and hydraulic features of the training image. The methodology consists of 3 basic steps: (1) a replication process that generates 2D stochastic DFNs from a 2D training image, (2) an upscaling process to generate CPMs out of the generated DFNs and (3) an extrusion process to stack the CPMs in 3D. These steps are presented in detail below. An exemplary simulation is used to illustrate them. A DFN out of a sensitivity analysis of the extent and shape of the EDZ to in-situ stress conditions around the structures of a geological repository[32] is used as training image (Fig. 1). The main inputs/outputs of such simulation are summarized in Table 1. The DFN is characterized by dominating elongated pseudo-horizontal fractures associated with bedding planes, as observed in Fig. 1e (though made of hundreds of smaller connected patches defined by four-point polygons; Fig. 1d) at the top and bottom of the gallery and some subsets of pseudo-vertical smaller features to the left and right. Apertures, and correspondingly transmissivities, as calculated using a cubic law, are relatively high and log-normally distributed around a mean value of 1 mm (Fig. 1c). For illustration purposes, we present one 3D simulation of the EDZ around a 25 m long, 3 m diameter gallery.

2.1. Stochastic generation of fracture networks

Following Xu & Dowd,[28] the scanning of fracture density, clustering and geometric properties (to be inherited by the simulations) of the training image is done over a specified super-block grid. The choice of the super-block size has an impact on the quality of the simulation and will be further explored in Section 2.4. Fig. 2

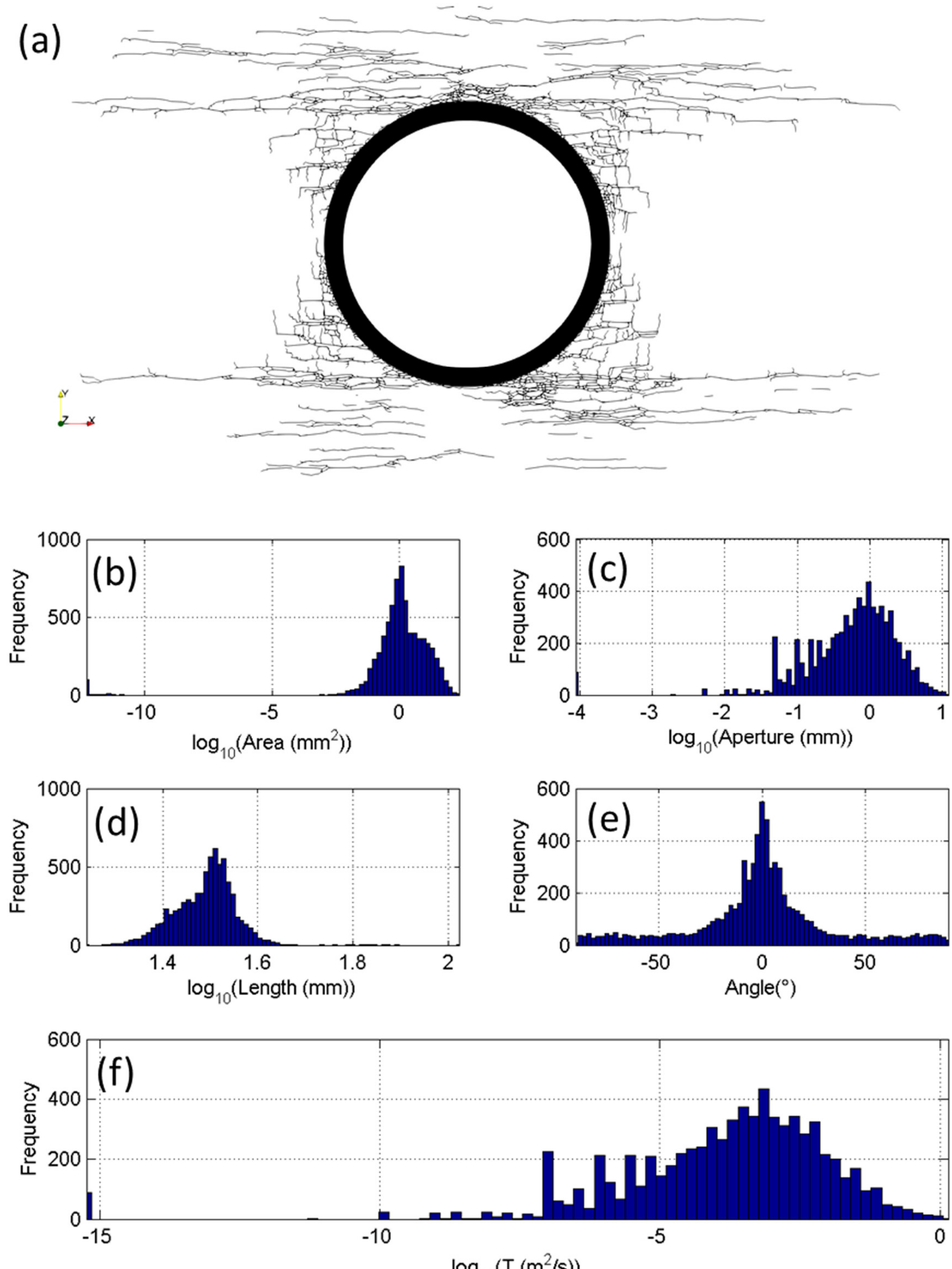

Fig. 1. (a) Discrete fracture network used as training image to illustrate the workflow.[32] The inner shell depicts the shotcrete around the gallery. (b) to (f) Histograms of patch area, aperture, length, orientation (counterclockwise from positive x-axis) and transmissivity, as derived by the cubic law from aperture.

displays the 50 × 50 super-block grid used in this illustrative example. Super-blocks completely inside the circumference defining the wall-rock contact are excluded from the scanning, which leads to considerable CPU savings.

First, fractures in the training image are replaced by a representative point (i.e. the centroid) and fracture intensity (or density, defined as number of centroids at each super-block) of the training image is mapped onto the super-block grid (Fig. 2). The mapped distribution is termed *I(i,j)*, where '*i*' and '*j*' are the indexes of the super-block at column '*i*' and row '*j*'. If more than one fracture category is considered (presenting e.g. different preferential orientations, break modes, etc.), the mapping is carried out individually, leading to different intensity maps $I_k(i,j)$, where k is the category index. In the simulation domain, and at each super-block, fracture centroids are located according to a homogeneous Poisson process describing a point pattern with complete spatial randomness.[33]

Table 1
Basic description of the training image used to illustrate the workflow.[6,32] The term "fracture patch" refers to small entities lumped into larger structures.

DFN HAA-23. Model inputs	
Tunnel diameter (m)	3
Shotcrete thickness (m)	0.2
Maximum in-plane principal stress (MPa)	20.7
Minimum in-plane principal stress (MPa)	15.9
Direction of maximum principal stress	Horizontal
Strength properties	
Host rock	Opalinus Clay
Tensile strength in horizontal/vertical directions (MPa)	8/1.28
Cohesion in horizontal/vertical directions (MPa)	3.8/68.8
Mode I fracture energy in horizontal/vertical directions (J m^{-2})	56/20
Mode II fracture energy in horizontal/vertical directions (J m^{-2})	160/560
Elastic modulus of support [MPa]	32
Core softening ratio (related to liner stiffness)	0.008
DFN HAA-23. Model outputs. Features of fracture patches	
Number	7378
Mean initial aperture [mm]	0.71
Mean length [mm]	31.56
Mean orientation [°]	0
Mean initial area [mm^2]	1.21
Mean initial transmissivity (log10) [m^2/s]	−3.54

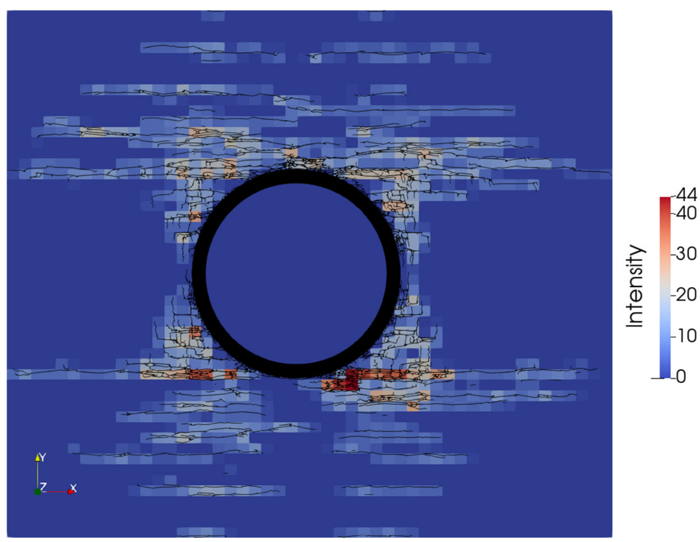

Fig. 2. 50 × 50 super-block grid and intensity map of the training image.

Yet, the algorithm is generic and can accommodate other statistical distributions and sampling methods at this stage. For instance, Xu & Dowd[28] implemented non-homogeneous, cluster and Cox sampling methods (see Ref. 34 for a review).

Fracture properties (i.e., length, aperture and orientation) are scanned within each super-block of the training image. The main outcomes of the scanning are the cumulative distribution functions (cdfs) for each property and super-block. Such cdfs are then randomly sampled to generate fracture properties (so-called point "marks") within the corresponding super-block of the simulation domain. Xu & Dowd[28] sample cdfs individually, what may lead to a significant loss of geometric coherence between fractures in the training image and in the simulations. For instance, long fractures may be distributed along the horizontal direction in the training image, but the individual sampling of length and orientation may generate such fractures along the vertical direction in the simulation domain. This problem can be alleviated by considering different fracture categories. However, the definition of such categories is somewhat arbitrary and does not completely solve the problem. Instead, a novel scanning method has been implemented, in which a "principal" property (orientation in this example) is defined as main driver of fracture geometry. The principal property is randomly sampled from the corresponding cdf and the fracture in the super-block of the training image with most similar value is identified. The remaining properties (length and aperture in this case) are directly copied from the identified fracture. The algorithm can be easily updated to accommodate a second principal property by considering concatenated sampling of cdfs. Once each generated centroid has been attributed with a length L, aperture b and orientation θ, a four-point polygon can be generated (Fig. 3):

(1) Generate two orthogonal unit vectors according to the fracture orientation θ [rad]:

$$\boldsymbol{u_1} = (\cos\theta, \sin\theta)$$
$$\boldsymbol{u_2} = (-\sin\theta, \cos\theta)$$

(2) Generate the mid points of fracture shortest edges $\boldsymbol{P_1}$–$\boldsymbol{P_4}$ and $\boldsymbol{P_2}$–$\boldsymbol{P_3}$ (points $\boldsymbol{M_{14}}$ and $\boldsymbol{M_{23}}$) using the fracture centre $\boldsymbol{C}$ as reference point and the fracture length L:

$$\boldsymbol{M_{14}} = \boldsymbol{C} + L/2 \cdot \boldsymbol{u_1}$$
$$\boldsymbol{M_{23}} = \boldsymbol{C} - L/2 \cdot \boldsymbol{u_1}$$

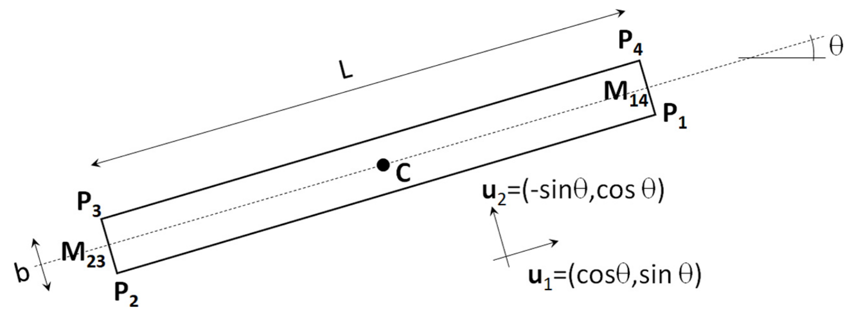

Fig. 3. Sketch of a four-point polygon defining a simulated fracture.

(3) Generate the rectangle from the fracture aperture b using $\boldsymbol{M_{14}}$ and $\boldsymbol{M_{23}}$ as reference points:

$$\boldsymbol{P_1} = \boldsymbol{M_{14}} - b/2 \cdot \boldsymbol{u_2};\ \boldsymbol{P_4} = \boldsymbol{M_{14}} + b/2 \cdot \boldsymbol{u_2}$$
$$\boldsymbol{P_2} = \boldsymbol{M_{23}} - b/2 \cdot \boldsymbol{u_2};\ \boldsymbol{P_3} = \boldsymbol{M_{23}} + b/2 \cdot \boldsymbol{u_2}$$

According to this formulation, fracture patches are represented by primitive rectangles. As an option, a random noise can be applied to the location of the four points to deform the polygon while keeping the sampled or derived geometric properties. Once the polygon is generated, a first consistency check is carried out. If the four points are inside the gallery, the fracture centroid and corresponding properties are re-simulated. Fractures intersecting the liner (black circumference in Fig. 2) are kept, but polygons are reconstructed to honour the intersection and fracture properties are recalculated accordingly. Therefore, the inheritance of the statistics of the training image is lost in this case. Fracture reconstruction occurs seldom and only at super-blocks at the rim of the gallery. In the current simulation, only 83 fractures out of more than 7000 had to be reconstructed. Thus, the loss of statistical coherence is minor and the quality of the reproduction of the statistics of the training image is not affected.

Random sampling of fracture location and properties may lead to significant fracture overlapping. This precludes the use of any "box-counting" technique for upscaling[5,6] (see Section 2.2). Thus, a thorough consistency check of overlaps between simulated fractures must be made to get rid of artificially high porosities/transmissivities. A spiral contact detection method[35] has been implemented to that end, according to which a generated fracture in a certain super-block is cross-checked with (1) all other previously generated fractures within the super-block and (2) with all other fractures in adjacent (and previously simulated) super-blocks. Once overlaps have been detected, corresponding fracture properties must be recalculated. There are two alternatives to tackle this problem, i.e., fracture resampling or reconstruction to avoid overlaps. "Brute force" resampling is hard to achieve if the intensity at the super-block is high (or if the super-block is small or both) because there is little room to place new fractures, which leads to high CPU consumption due to the many resampling attempts. In addition, it hinders fracture connectivity since fracture intersections are not allowed. Instead, reconstruction is easy to implement, but the statistics of the simulated fracture properties are not exactly consistent with those of the training image. In this example, and for simplicity, we simply resample overlapping fractures.

Fig. 4 displays a comparison between the training image and a randomly generated DFN. As observed, the long horizontal features characterizing the training image are not clearly present in the simulation. Such long features in the training image are not individual lumped entities but made of several (sometimes hundreds) smaller fracture patches. Therefore, the sampling process generates unconnected fracture patches with coherent stochastic properties. In nature, EDZ fractures nucleate and grow around (or from) previously generated fractures. This behaviour cannot be reproduced by a purely statistical algorithm (despite it draws on geomechanical simulations). The apparent loss of connectivity can be alleviated by reconstructing overlapping fractures instead of resampling them. Never the less, after upscaling (see Section 2.2) the simulated DFN, the conductive features of the small individual fracture patches will be integrated in an equivalent continuum porous medium model that captures the overall hydraulic connectivity and significance of the original elongated feature. Since flow simulations will be supported by the CPM and not by the simulated DFNs, the loss of geometric connectivity is only a minor issue.

The reproduction of the statistics of the training image is displayed in Fig. 5. As observed, the statistics of the geometric properties of the training image are preserved. Only some small divergences are observed in the cdf of fracture orientation (Fig. 5b). These can be attributed to the cropping of fractures intersecting the liner or to the use of a large number of super-blocks. Super-blocks far away from the gallery are insufficiently populated with fractures and therefore the quality of the cdf of the training image is poor, so is its reproduction in the simulation.

2.2. Upscaling to equivalent continuum models

The upscaling process from DFN to equivalent CPM has been described in detail in Alcolea et al.[6,36] and is summarized in Fig. 6. In short, a finite element mesh is superimposed to the simulated DFN and fracture properties are mapped and converted to hydraulic properties (hydraulic conductivity and porosity) attributing each mesh element (Fig. 6b). Given that the flow towards the gallery is pseudo-radial during the resaturation phase, the selected grid resembles radial flow conditions. Next, abstractions of the EDZ (in the sense of simplified shell-like models) (Fig. 6c) and fluid flow simulations mimicking e.g. the resaturation of the system can be carried out.

Fig. 7 displays the upscaled porosity fields of the training image and the simulation in Fig. 4. As observed, the geometric patterns of the upscaled field are very similar to those of the upscaled training image. Indeed, some differences between them are observed (up to 6% in this case), mainly at areas where fracture intensity is the highest. Even though the "geometric" connectivity of the training image (made of a few pseudo-horizontal elongated features) is not resembled by the simulated DFN (made of many disconnected features), the hydraulic significance of the EDZ depicted in the training image is inherited by the simulations after upscaling the corresponding CPMs, both in axial and radial directions. Radial flow conditions are addressed by simulating the transient resaturation of the system. Fig. 8 displays the excellent reproduction of the radially integrated axial fluxes, porosity and fracture density distributions, and the temporal evolution of the storativity of the system.

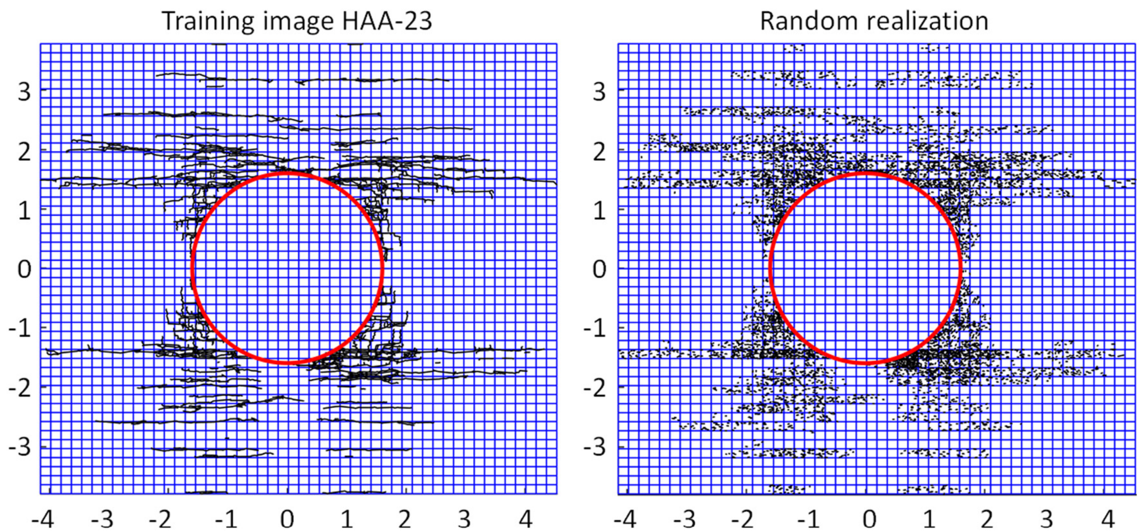

Fig. 4. Comparison between the training image and a random simulation. Super-block grid is depicted with blue lines.

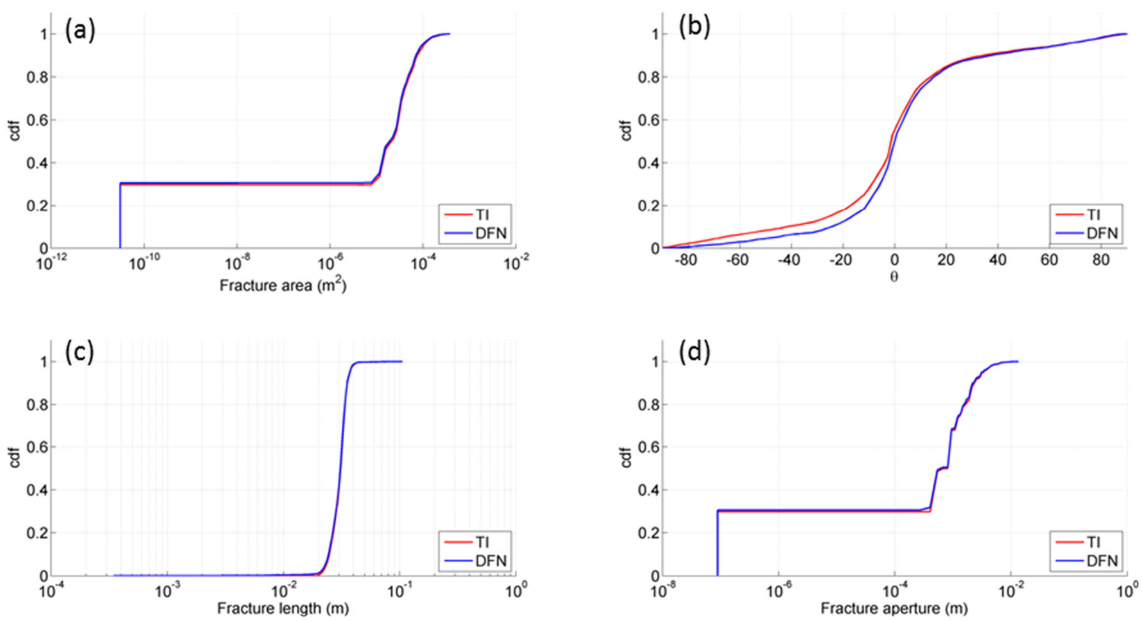

Fig. 5. Comparison between the cdfs of fracture properties defining the training image and the simulation in Fig. 4: (a) fracture area, as derived from (b) fracture orientation counterclockwise from positive *x*-axis, (c) fracture length and (d) fracture aperture. Note the semi-logarithmic scales in panels (a), (c) and (d).

Small differences in integrated porosities are found only at short radial distances, likely caused by the reconstruction of fractures intersecting the liner. Still, global trends are honoured. The same can be observed with regards to the integrated distribution of hydraulic conductivity (not displayed here).

To make the long story short, a set of geometrically coherent DFNs and corresponding hydraulically equivalent CPMs have been simulated from the original DFN taken as training image. Thus, the suggested approach relies on the validity of the DFNs, which are calculated under the assumption of plane stress. This is supported by empirical evidences from EDZ investigations in URLs (e.g. Mont Terri in Switzerland, Bure in France), including the inspection of core maps from EDZ boreholes and trace mapping at the tunnel surface. In their synopsis of EDZ phenomena in URLs, Lanyon et al.[37] provide a survey of empirical data bases and conceptual models of the EDZ. Plane stress conditions are reported as a valid first order assumption. In the more detailed appraisals the speed of the excavation process and the lining measures have an additional impact on the EDZ initiation and propagation, causing more complex 3-D fracture patterns. In spite of the validity of the planar stress assumption, 2D flow simulations based on equivalent CPMs (or on DFNs) tend to overestimate the flux along the EDZ, because continuity of the axial flow paths is assumed. In order to avoid such artefacts, the suggested approach mimics the break of axial continuity of the EDZ fracture system by connecting 2-D representations of a stochastic EDZ network in a piecewise manner.

2.3. 3D stacking

The simulated DFNs are defined over a cross-section orthogonal to the gallery axis and are simulated independently. The 2D mesh

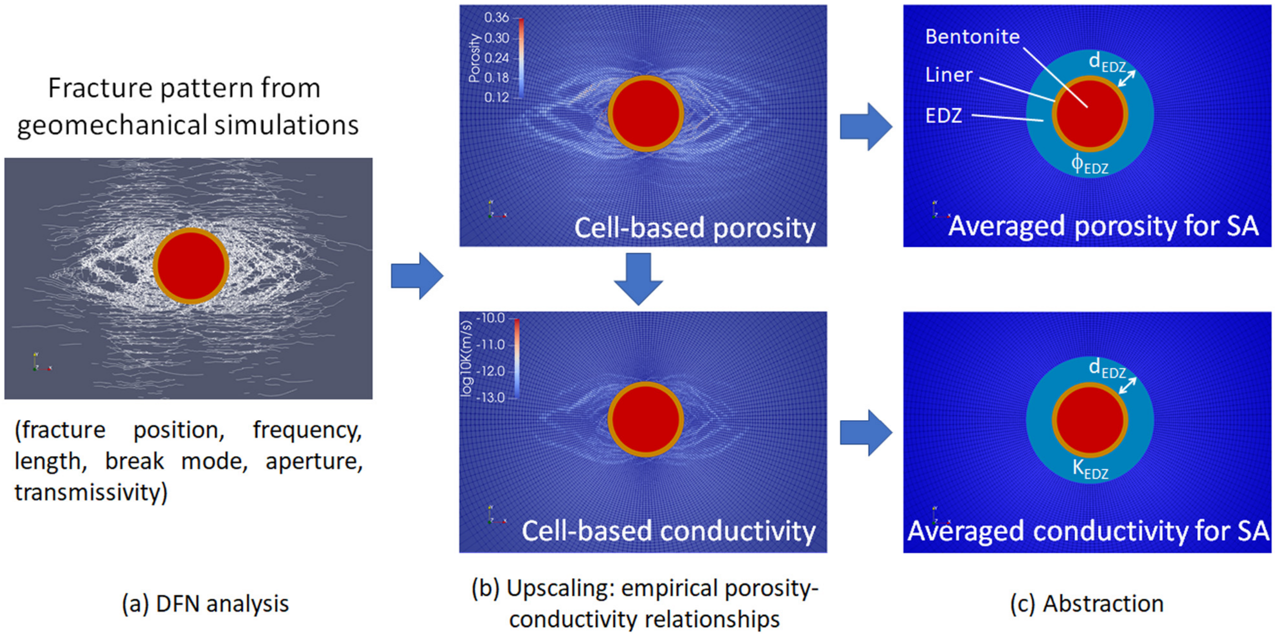

Fig. 6. Upscaling and abstraction process of the EDZ: (a) DFN depicting representative fracture patterns that mimic the excavation process; (b) the discrete fracture patterns are converted into heterogeneous distributions of porosity and hydraulic conductivity; and (c) in a final abstraction process, the heterogeneous distributions are converted into a shell-like simplified model defined by radii and homogeneous, hydraulically equivalent values of porosity and hydraulic conductivity.
Source: From Ref. 6.

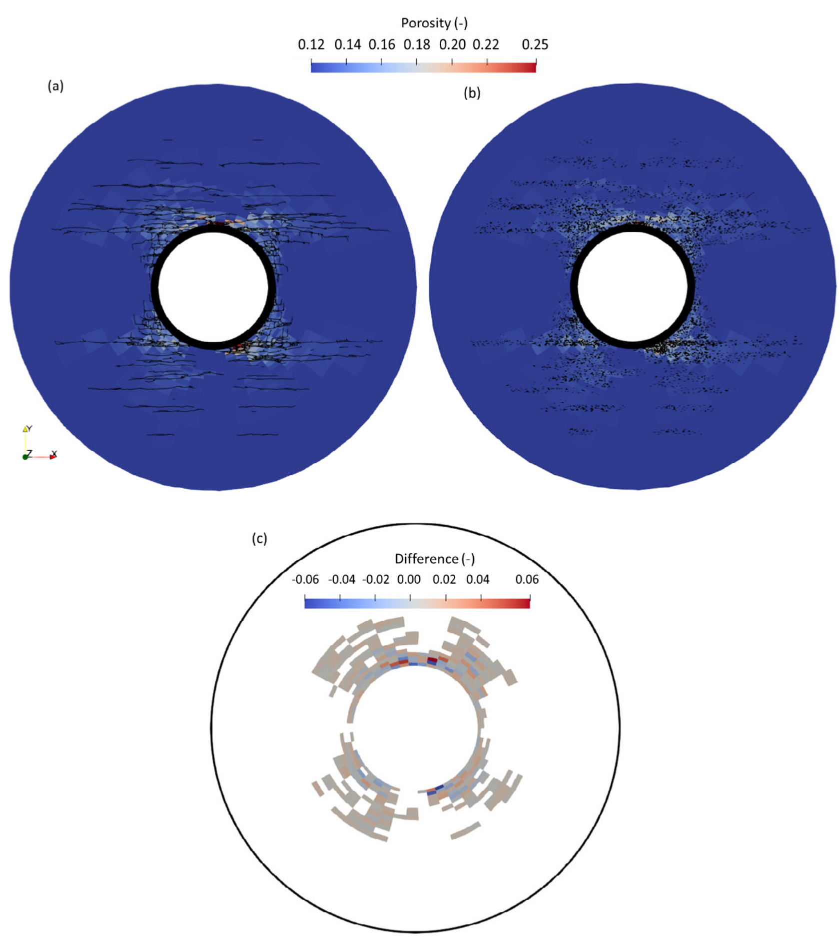

Fig. 7. Upscaled porosity fields of (a) training image and (b) simulation. Panel (c) displays the difference between them.

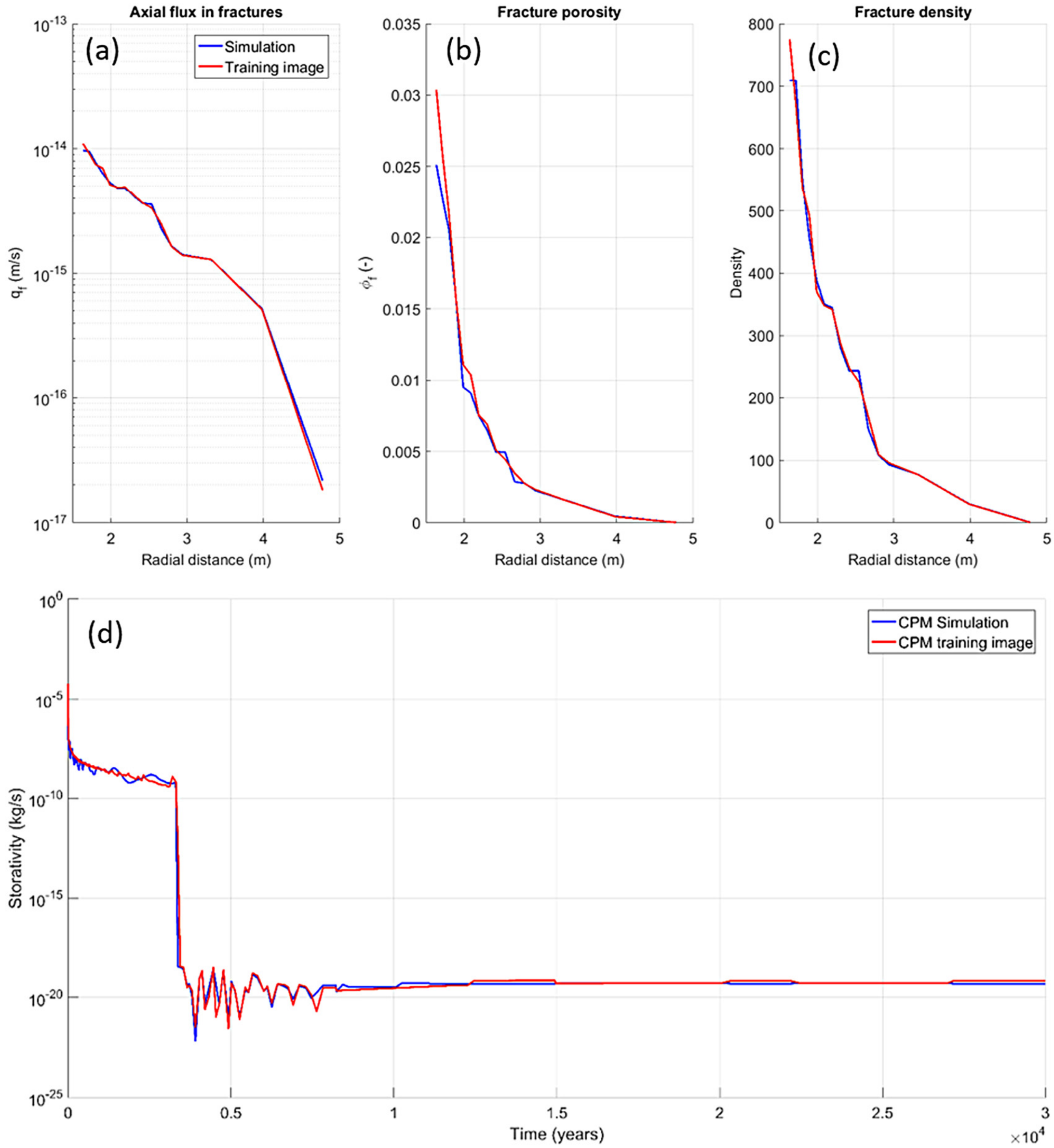

Fig. 8. Comparison between the hydraulic significance of the training image (red lines) and of the simulation (in blue). (a) radially integrated axial fluxes: axial significance. The procedure for radial integration is described in Ref. 36; (b) Integrated fracture porosity; (c) Integrated fracture density; (d) temporal evolution of the storativity of the system under resaturation conditions.

used for the upscaling of simulated DFN properties is first extruded in the direction orthogonal to the plane of the simulation. For illustration purposes, we simulate a 25 m long gallery using 5 slices with element length 5 m. Five different stochastic simulations of the EDZ are generated according to step 1 and upscaled to hydraulically equivalent CPMs according to step 2 of the methodology. The CPMs are stacked in the direction parallel to the gallery axis in a random manner by simple "shuffling", which leads to different simulations of the 3D geometry of the EDZ that are coherent with the 2D patterns defined by the training image (Fig. 9). This extrusion method presents advantages and drawbacks. The drawback is that the connectivity structure of the EDZ along the direction of excavation is not accommodated. For simplicity, we have assumed that fracture length along the orthogonal direction is smaller than the element length (<5 m in this example). This assumption is supported by the EH experiment in Mont Terri,[38,39] which showed that transmissive EDZ fractures were smaller than 1 m in extent. Advantages are (1) the ease of implementation, (2) enhanced speed and (3) the method can consider different training images (e.g. mimicking different rock strength conditions) at different sections of the gallery, thus accommodating hardening/weakening conditions caused by the excavation process. A way to tackle the connectivity problem consists of sampling an additional cdf depicting fracture length along the direction parallel to the gallery and perform steps 1 and 2 in three dimensions directly. The definition of such cdf needs to be based on physical evidence such as fracture trace maps at the tunnel wall. Due to the lack of such data, we have chosen the stacking of independent 2D simulations for simplicity. Yet, the algorithm is generic and can easily accommodate this option.

2.4. Impact of the number of super-blocks

The choice of the super-block size has an impact on both the CPU consumption and on the quality of the simulated DFNs in step 1. Besides feasibility considerations, the number of super-blocks mainly controls the quality of pattern reproduction in two different ways. A small number of super-blocks leads to a slightly

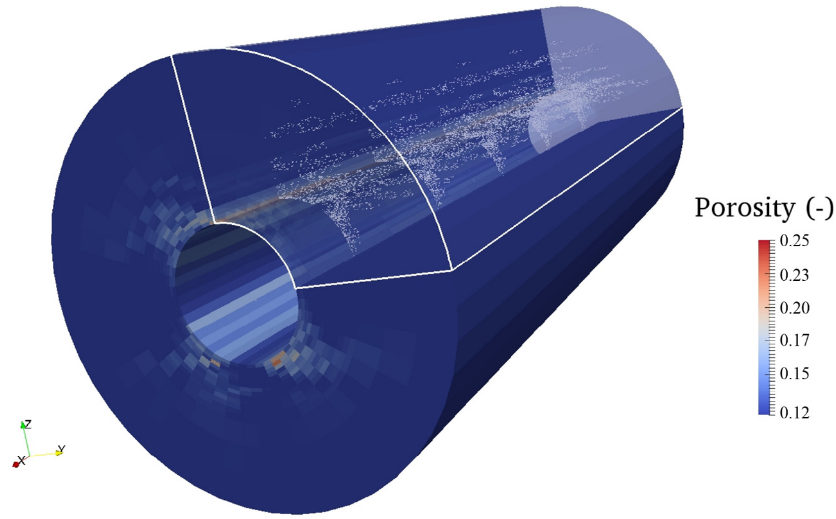

Fig. 9. One realization of the stacked 3D equivalent continuum porous model. The fracture network is partly visible (quadrant 12 o'clock to 3 o'clock, encompassed by white lines; the opacity of the porosity distribution has been reduced 50% there).

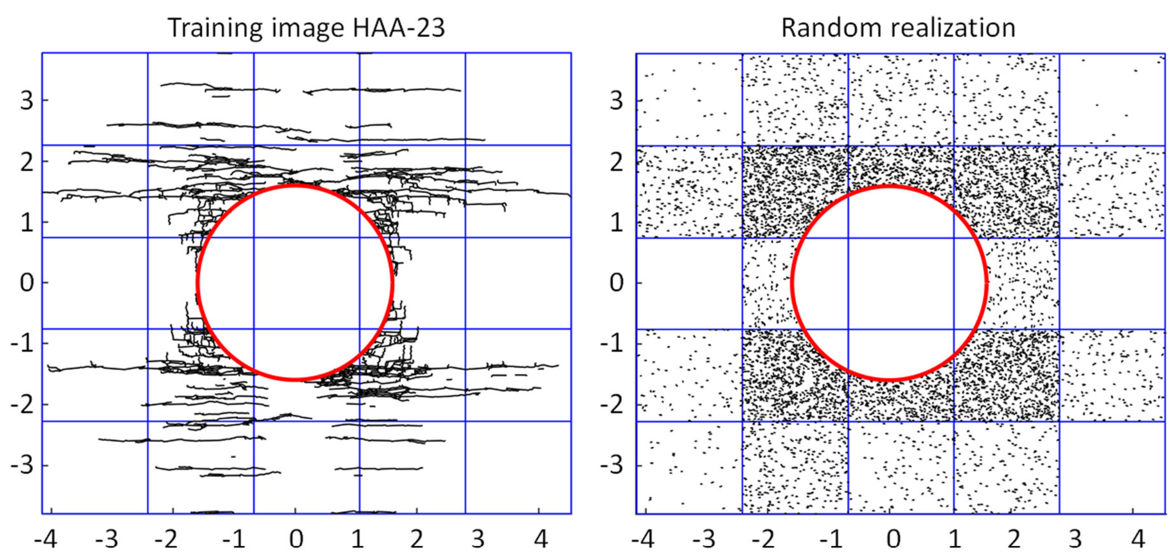

Fig. 10. Training image (left) and simulated fracture network using a 5 × 5 super-blocks grid. The wall-rock contact is depicted by a red line and the super-blocks are depicted in blue.

better reproduction of the cdfs of the training image. However, the reproduction of geometric patterns is poor. In fact, if just one super-block is considered, the point process is completely random because the intensity is the total number of fractures in the training image. Thus, one can expect a "blurred" and sparse distribution of the simulated fracture network, not resembling the geometric patterns of the training image. Fig. 10 displays a simulation using a 5 × 5 super-block grid. As observed, the reproduction of geometric patterns is worse than that in Fig. 4. This results in a poorly upscaled CPM and, correspondingly, the integrated distributions of axial flux and fracture porosity and density differ much from the corresponding ones in the training image (Fig. 11). Consequently, the super-block size must be optimally chosen to (1) reproduce correctly the geometric patterns of the conceptual model depicted by the training image, (2) reproduce correctly the statistics of the training image, expressed in terms of cdfs of fracture length, orientation and aperture and, (3) keep the CPU effort under tolerable limits. CPU times were 2 and 4 h for the 5 × 5 and 50 × 50 super-block grids respectively (HP Z200 Workstation). An exhaustive sensitivity analysis to the super-block size is out of the scope of this paper.

3. Application. The multi-rate injection test of the HG-A experiment in Mont Terri

The methodology is benchmarked with a data set from the HG-A experiment ("Gas path through host rock and along seal sections, HG-A"), an in-situ self-sealing experiment at the Mont Terri Underground Rock Laboratory (URL) in Switzerland. The HG-A experiment provides an extensive database on the EDZ behaviour that has been used in previous modelling tasks.[40,41]

A 1 m-diameter, 13 m-long microtunnel was excavated during February 2005 from a niche in Gallery 04 of the URL. The microtunnel was excavated parallel to the strike of bedding planes dipping at about 50°, thus replicating the expected relationship between bedding and emplacement tunnel orientation in a deep repository.[42] The first 6 m of the microtunnel were lined with a steel casing immediately after excavation to stabilize the opening. The gap behind the liner was then cement-grouted, but not sealed. A purpose-built hydraulic megapacker (diameter 940 mm and sealing section length 3000 mm) was installed in 2006. The sealing section was located at 6–9 m with a 1 m grouted zone

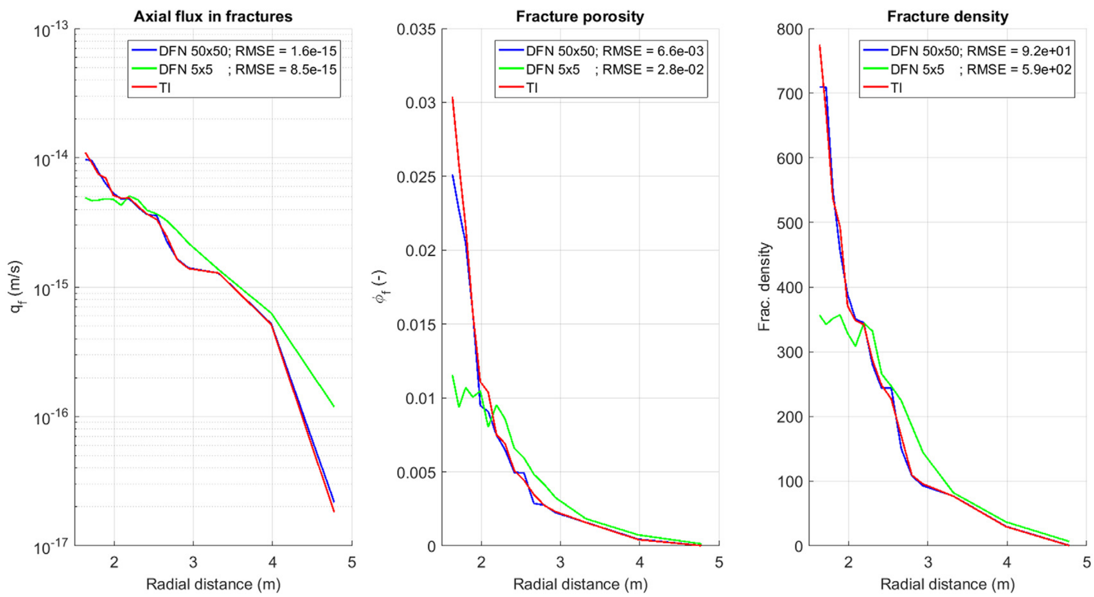

Fig. 11. Comparison between the radially integrated porosities of the training image (red lines) and of the simulations generated using 50×50 and 5×5 super-blocks grids (in blue and green respectively). In the insets, RMSE denotes the root mean square difference of the cdfs of simulation and training image.

Table 2
Main features of the discrete fracture networks and corresponding mechanical parameters used in the modelling of the HG-A experiment.
Source: Modified from Geomechanica.[45]

Simulation	Maximum in-plane principal stress (MPa)	Minimum in-plane principal stress (MPa)	Dip of the maximum principal stress direction (°)
HG-A	6.5	4.5	90 (vertical)
HG-A-F	6.5	4.5	90 (vertical)
HG-A-S1	6.5	4.5	140 (perpendicular to bedding)
HG-A-S2	6.5	4.5	50 (parallel to bedding)
HG-A-S3	5.5	5.5	(Isotropic stress)
HG-A-S4	6.5	6.5	(Isotropic stress)
Triangular elements (rock matrix)			
Bulk density (kg/m^3)			2430
Young's modulus ∥ to bedding (GPa)			10
Young's modulus ⊥ to bedding (GPa)			4
Poisson's ratio ∥ to bedding			0.35
Poisson's ratio ⊥ to bedding			0.25
Shear modulus ⊥ to bedding			3.6
Viscous damping coefficient (kg/m s)			$1.25 \cdot 10^5$
Crack elements			
Tensile strength ∥ to bedding (MPa)			1.8
Tensile strength ⊥ to bedding (MPa)			0.44
Cohesion parallel to bedding (MPa)			2.8
Cohesion ⊥ to bedding (MPa)			24.8
Mode I fracture energy ∥ to bedding (specific; J/m^2)			19.5
Mode I fracture energy ⊥ to bedding (specific; J/m^2)			1.0
Mode II fracture energy ∥ to bedding (specific; J/m^2)			27.5
Mode II fracture energy ⊥ to bedding (specific; J/m^2)			96.5
Friction angle of intact material (°)			22
Fracture penalty (GPa)			35
Interaction parameters			
Friction angle of fractures (°)			22
Normal contact penalty (GPa m)			70
Tangential contact penalty (GPa m)			70

containing the non-sealing part of the packer and retaining wall from 9–10 m. The final 3 m of the microtunnel from 10–13 m form the test section which was instrumented and backfilled prior to megapacker emplacement (Fig. 12; see Ref. 44 for further details).

The EDZ around the microtunnel is formed by the interaction of the rock and stress anisotropy with significant breakout zones ('notches') at 3 o'clock and 9–11 o'clock, where the SSE-dipping faults and the bedding planes are approximately tangent to the excavation boundary. According to Geomechanica,[45] the development of failure at these locations can be explained by the lower strength of the bedding planes and tectonic faults, which tend to favour shear failure under the effect of the excavation-induced stress redistribution. In the upper-left wall, buckling phenomena tend to form slab-like breakouts, while in the lower-right wall the damage appears to be prevalently stress-controlled, with the formation of extensional fractures associated with the minor in-plane principal stress.[46] Furthermore, the faults oblique to the bedding tend to act as a boundary to the propagation of fractures. The asymmetry in the EDZ shape may be explained by (i) a lower discontinuity frequency in the SSE-dipping fault system in the

Table 3
Temporal sequence. Sequence 5 of gas injection is not considered in the modelling exercise. The last five columns refer to the zonation in Fig. 12.

Sequence	Model	Description	Initial date	End date	Open	Seal	Grout	Test	OPA
1	1	Excavation	1.3.2005	11.3.2005	Hole	Hole	Hole	Hole	Filled
2	2	Emplacement	11.3.2005	31.10.2006	Hole	Filled	Filled	Filled	Filled
3	2	Resaturation	31.10.2006	1.2.2008	Hole	Filled	Filled	Filled	Filled
4	2	Hydraulic test	1.2.2008	1.2.2010	Hole	Filled	Filled	Filled	Filled
5	2	Gas injection	1.2.2010	1.10.2011	Hole	Filled	Filled	Filled	Filled

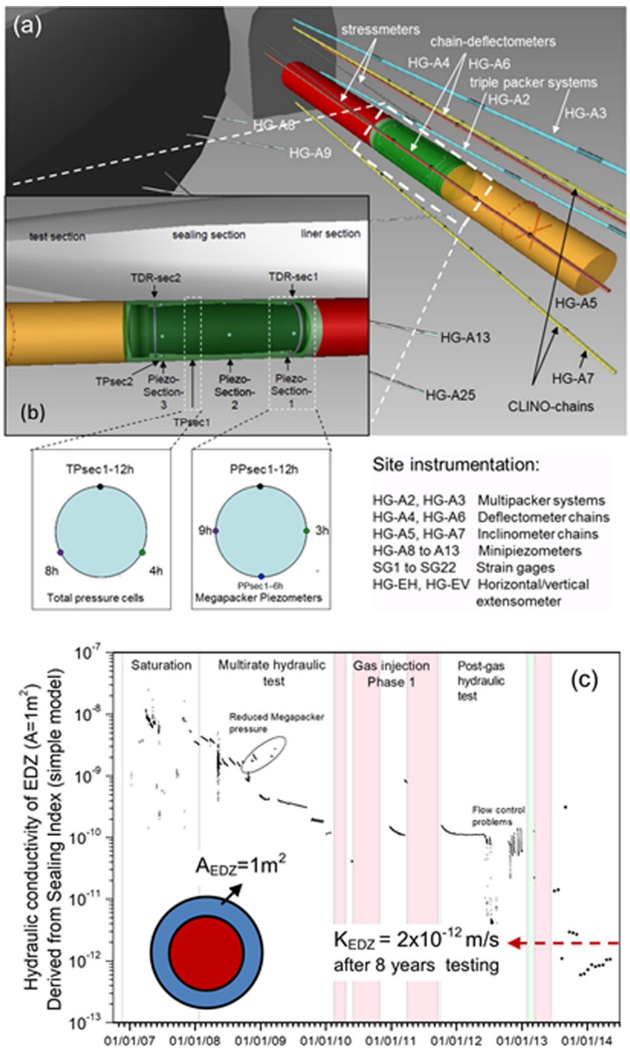

Fig. 12. The HG-A experiment in the Mont Terri URL. (a and b) Layout and borehole instrumentation (colour coding refers to the steel liner, red; the seal section, green; and the backfilled test section, orange; from Ref. 42); (c) Sealing index[41] observed during the HG-A experiment. A significant reduction in the ability to inject water into the Test Section caused by the sealing of the EDZ conductive features is observed. At the end of the observation period, the effective hydraulic conductivity of an equivalent radial double shell EDZ model with a cross-sectional area of 1 m^2 is around 2 · 10–12 m/s; from Ref. 43.

bottom part of the tunnel and (ii) the confining effect provided by the debris kept in place under the effect of gravity. Within the seal section, prior to emplacement of the packer the original tunnel profile was restored by backfilling the breakouts with cement.

Saturation of the test section and surrounding rock started in November 2006 following the emplacement of the megapacker (June 2006). Subsequent injections during 2007 showed an ongoing reduction in system storage, presumably due to dissolution of trapped air in the test section and resaturation of the EDZ. An extended multi-rate injection test was initiated in January 2008 after a two months recovery period (summer 2007) and some other minor injections. The gas injection phase included three separate nitrogen gas injections and started in February 2010 (see Ref. 47 for further details). The analysis of the gas injection is out of the scope of this paper.

3.1. Model setup

Six geomechanical simulations mimicking the excavation process, with varying stress tensor are reported by Geomechanica[45] and are summarized in Table 2. These simulations are used as training images to calibrate the pressure data sets recorded by the observation sensors in Fig. 12. The software iTHOUGH2[48,49] is used to that end.

The model considers the open, seal, grouted and test sections, and 2 m of intact Opalinus Clay ahead of the test section to account for the low hydraulic conductivity of the formation. Along the microtunnel axis, the model is discretized by 50 orthogonal slices, with spacing varying between 1 and 90 cm. The finite element mesh consists of 12 480 nodes and 11 376 elements and has been refined longitudinally at the test section, near the niche and at the contact between the different sections (Fig. 13). The refinements at the test section and near the niche are necessary to avoid numerical instabilities at areas near the boundary conditions. At the contacts between sections, where a sudden change in the EDZ geometry may occur, longitudinal refinement is also necessary.

The temporal sequence of the HG-A experiment, up to the gas injection, is implemented in the model. Two stages are modelled separately using two different model topologies. (Table 3). The excavation process and the corresponding desaturation is modelled first. It is assumed that the excavation process is instantaneous. Thus, the central part of the mesh is not implemented in the first model. Next, the backfilling of the test and grout sections and the emplacement of the mega-packer at the seal section are modelled. During these stages, a resaturation of the EDZ occurs. Finally, the multi-step hydraulic test is modelled. The last four stages of the temporal sequence are modelled together since the topology of the model does not vary after emplacement. iTHOUGH2 discretizes the time domain using a fully implicit first-order backward finite difference scheme. An initial minimum time step of 10^{-5} s is chosen. Yet, iTOUGH2 may increase/reduce it automatically depending on the convergence rate.

Boundary conditions for models 1 and 2 are sketched in Fig. 14. Note that step 2 in the modelling sequence, i.e., emplacement, included a long period when the complete tunnel was open.[47] This period, that implies a partial resaturation of the system has not been modelled here for simplicity. Nonetheless, the impact of partial resaturation on pressure evolution is small compared with that of fluid injection, described next. Step 4 in the temporal sequence involves a transient prescribed flow rate condition representing the injection at the test section (Fig. 15). The prescribed flow rate is applied at the central node of the cross section between the test section and the intact Opalinus Clay. The small frequency fluctuations of the injection sequence must be smeared a priori, since they would lead to numerical instabilities in the simulated pressure fields. To that end, we use the flow rate curve implemented by Lanyon & Senger.[9] As observed in Fig. 15, the hydraulic response at some observation points is almost immediate and shares the

Table 4
Model parameters. Calibrated parameters are the closure correction factor f, the closure rate α and the hydraulic conductivity of the grouted breakouts K_{grout}. For these parameters, the column value contains the prior information used in the calibration.

Notation	Description	Value	Reference
C_f	Fluid compressibility	$4.4 \cdot 10^{-10}$ Pa^{-1}	Fine and Millero[52]
C_s	Solid compressibility	$1.83 \cdot 10^{-9}$ Pa^{-1}	Poppei et al.[53]
μ	Fluid viscosity	10^{-3} Pa s	Lanyon and Senger[9]
ρ	Fluid density	10^3 kg/m^3	Lanyon and Senger[9]
g	Gravity	9.81 m/s^2	
p_{atm}	Atmospheric pressure	101325 Pa	
b_r	Irreducible aperture	8.9 10^{-8} m	Alcolea et al.[36,43]
ϕ_{OPA}	Total porosity of intact Opalinus Clay	0.12	Alcolea et al.[36,43]
K_{n0}	Stiffness	$920 \cdot 10^6$ Pa/m	Yong et al.[51]
K_{OPA}	Hydraulic conductivity of the intact Opalinus Clay	10^{-14}	Alcolea et al.[36,43]
f	Closure correction factor	1	
K_{grout}	Hydraulic conductivity of cement	10^{-15}	
α	Closure rate	−3.4	Alcolea et al.[43]
K_{axial}	Geometric mean of in-plane hydraulic conductivities		Alcolea et al.[43]

Table 5
Training images for different sections along the microtunnel. The referred HGA-simulations are displayed in Fig. 16. K_{OPA} denotes hydraulic conductivity of the intact Opalinus Clay.

Zone	Section	FEMDEM simulation
Open	0.0–2.0 m	HGA-S4
	2.0–4.0 m	HGA-S4
	4.0–6.0 m	HGA-S2
Seal	6.0–7.5 m	HGA-S1
	7.5–9.0 m	HGA-A-F
Grout	9.0–9.5 m	HGA-A-F
	9.5–10.0 m	HGA-S4
Test	10.0–11.5 m	HGA-S1
	11.5–13.0 m	HGA-S3
OPA	13–15 m	K_{OPA}

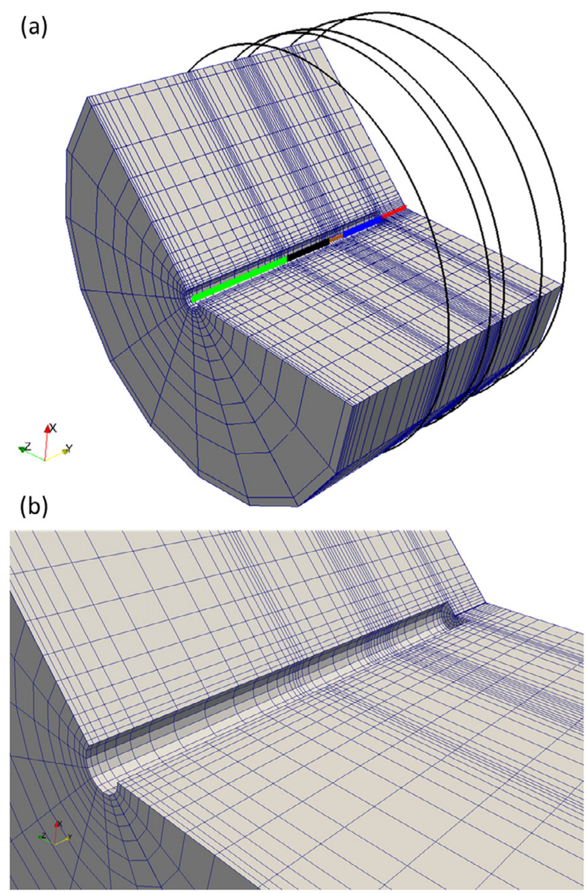

Fig. 13. 3D view of the finite element mesh, from the niche ($y = 0$) to the rear of the micro-tunnel. In the upper panel, black rings depict the different sections of the microtunnel. Colour coding in upper panel: green = open section; black = seal section; orange = grouted section; blue = test section; red = Opalinus Clay.

"spiky" trends of the curve depicting the injected flow rate. Indeed, smearing the boundary condition leads to a "softer" response of the system. In addition, the injected flow rate measured at early times is erratic and attributed to strong hydromechanical effects on pore pressure after excavation, as discussed in Refs. 46,50. This makes difficult to find an equivalent smeared injection volume. These issues impact negatively in the quality of the calibration presented here.

Initial conditions for model 1 are hydrostatic. Due to CPU issues, parameter calibration is not carried out for model 1. Instead, certain initial model parameters are assumed and model 1 is run. The pressure distribution at the last time step of model 1 serves as initial condition for model 2. Therefore, the initial condition for model 2 is highly uncertain and may not be coherent with the automatically updated parameters. This may lead to stark transitions between models 1 and 2, both in terms of pressure and spatial distributions of parameters. This problem is tackled by re-running model 1 after a few parameter updates of model 2. After a few iterations of this process, the parameter estimation is robust and the transition between models smooth.

The desaturation (sequence 1 in Table 3) or the resaturation of the system (sequence 3) and the multi-rate injection (sequence 4) lead to pressure variations and therefore, to changes in hydraulic conductivity and porosity of both fractures and matrix at the near field. Note that total porosity is assumed to be constant in time.[6] Resaturation causes two effects. On the one hand, a pressure increase in the EDZ leads to a reduction of effective normal stress and correspondingly to mechanical fracture closure and to a reduction of fracture porosity and hydraulic conductivity. On the other hand, the high content of clay minerals makes the rock matrix to swell, what leads to an increase of matrix hydraulic conductivity and porosity. Analogously, the multi-rate injection leads to pressure increase in the fractures with corresponding aperture increase. Temporal variations of hydraulic conductivity and porosity are accommodated in the model through a function relating fracture aperture b [L] and overpressure Δp [M L^{-1} T^{-2}] (i.e., pressure above

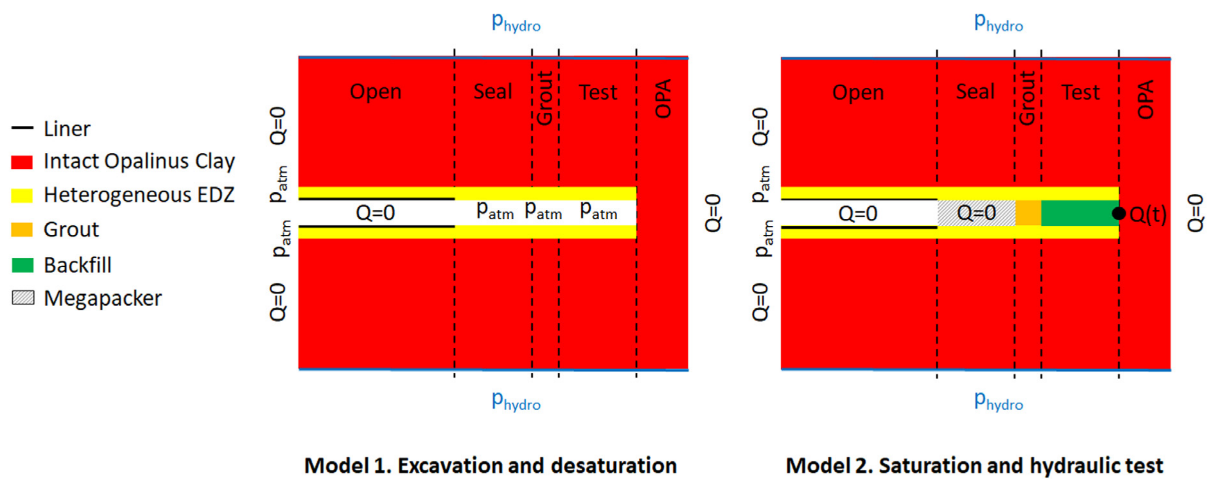

Fig. 14. Boundary conditions. The time function for the prescribed flow rate Q(t) at the contact between the test section and OPA is displayed in Fig. 15.

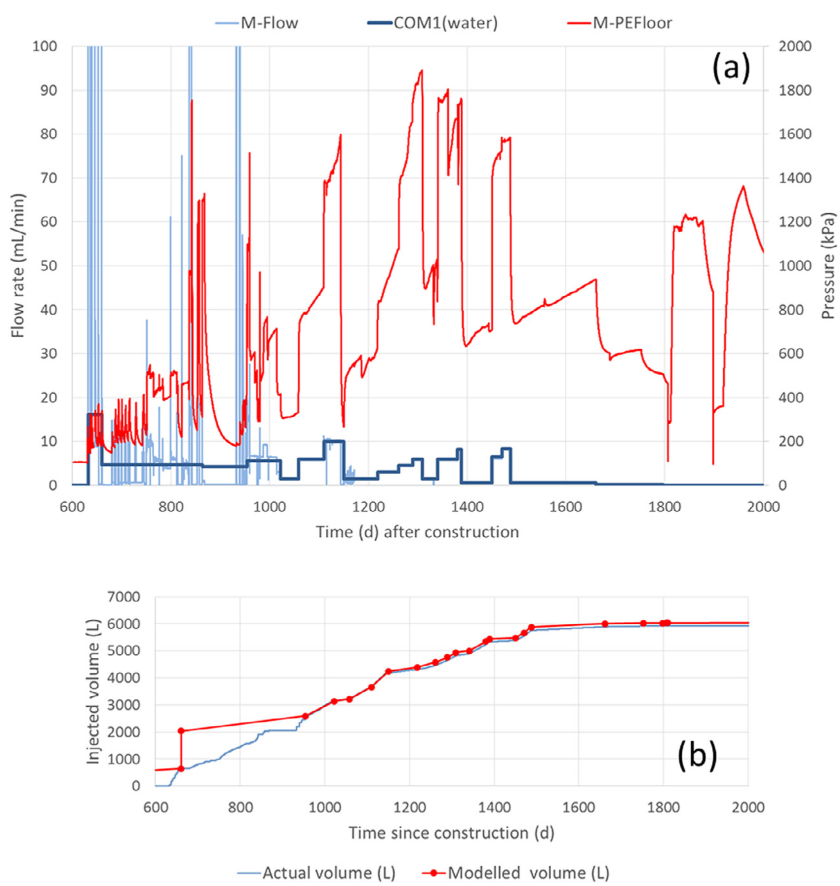

Fig. 15. (a) Prescribed flow rate at the test section during resaturation and hydraulic testing. The light blue curve (M-Flow) represents actual flow rate measurements. The thick blue line represents the implementation in iTOUGH2. The red line represents the pressure response at sensor M-PE-Floor; (b) Lower panel: measured and implemented cumulative injected volumes.

atmospheric; from Ref. 6):

$$b\left(p\left(t\right)\right)=b_0\left(1-\frac{1}{\left(b_0K_{n0}/\Delta p(t)\right)^{1-\alpha}+1}\right);\alpha<1 \qquad (1)$$

where b_0 is the initial fracture aperture [L] and K_{n0} ([M L^{-2} T^{-2}], ~920 M Pa m^{-1}; Ref. 51) is fracture normal stiffness. The exponent α [-] controls the velocity of fracture closure and is referred to as the closure rate. Low α values lead to smaller apertures for a given value of overpressure. The calculated apertures are then transformed to hydraulic conductivity and porosity according to Alcolea et al.[36] Additional parameters controlling the hydraulic behaviour of the system are the hydraulic conductivity and porosity of the intact Opalinus Clay (assumed to be constant in time) and the hydraulic conductivity of the cement used to jet-grout the breakouts around the gallery K_{grout}. A set of initial calibration runs revealed the need for calibrating an additional parameter, f [-] $\in$ [0,1], an overall correction factor for fracture closure. A value $f = 0$ represents that all fractures are closed and the hydraulic parameters are those of the intact Opalinus Clay. The

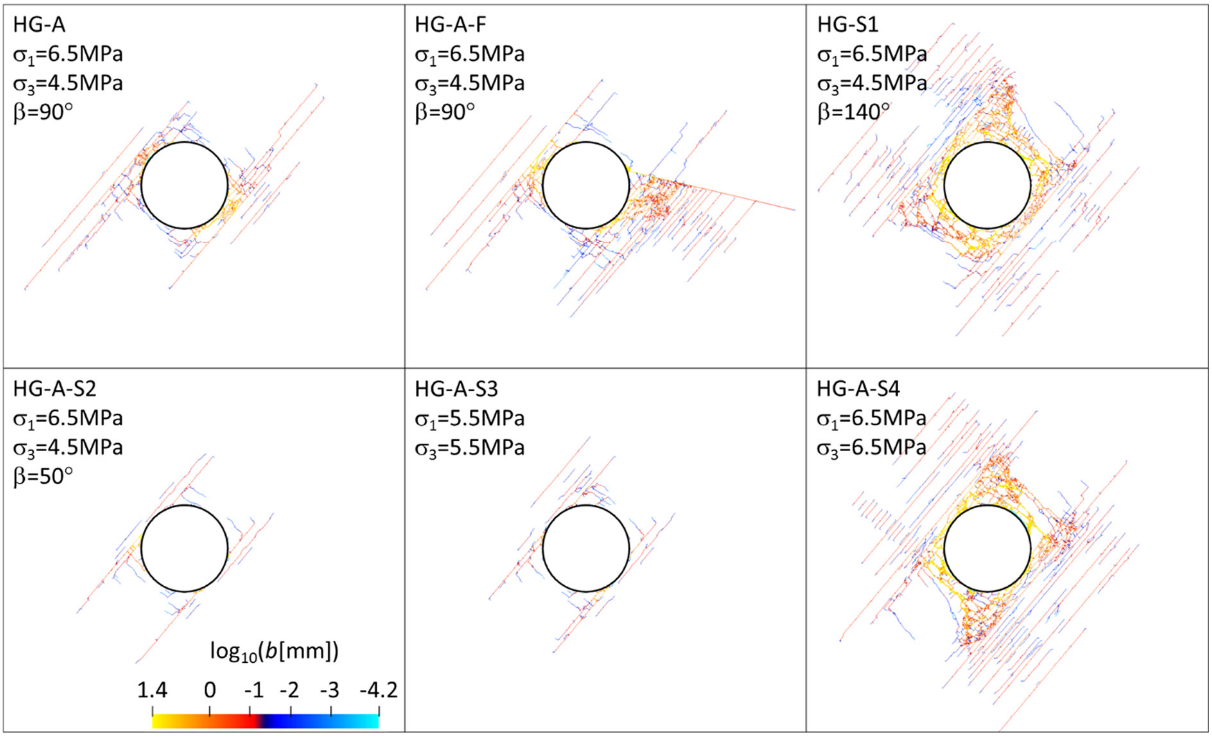

Fig. 16. Geomechanical simulations used as training images in the calibration analysis. σ_1 and σ_3 denote the maximum and minimum in-plane principal stresses. β denotes the dip of the σ_1. Bedding planes dip at 50° approximately. Colour coding refers to log10 of initial fracture aperture b. Simulation HG-A-F includes the presence of a natural fault. The black circle depicts the intersect of the gallery.

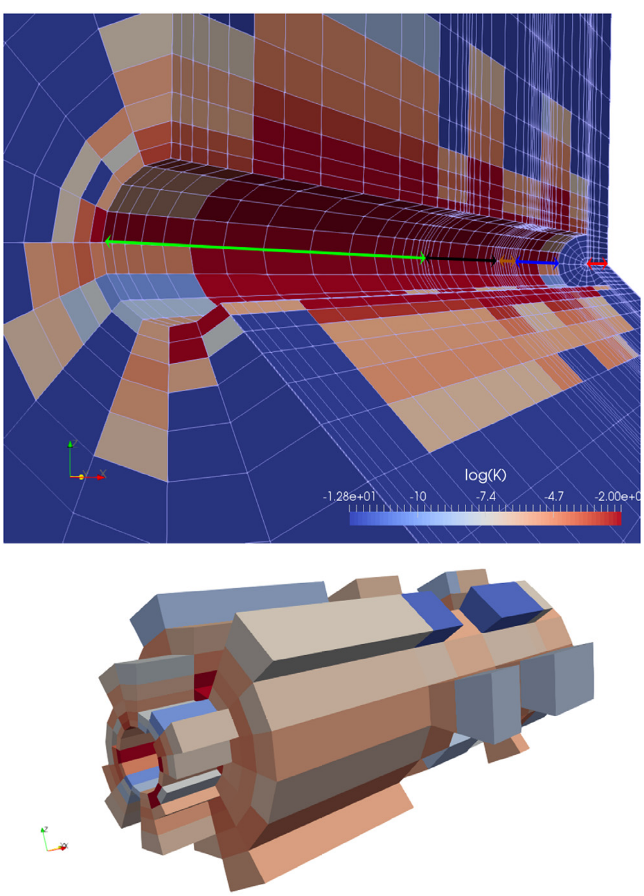

Fig. 17. Upper panel: overall view of the calibrated hydraulic conductivity field (in log10 scale) at early times after excavation. Colour codes depicting the different sections along the microtunnel refer to Fig. 13. Lower panel: view of the highly conductive features only.

remaining parameters are set to constant and known values along the calibration procedure and are summarized in Table 4.

The temporal variability of the hydraulic conductivity field is accommodated in the calibration procedure. Each iteration (i.e., update of model parameters) involves four basic steps:

(1) upscaling and stacking of the initial hydraulic conductivity field from the simulated DFNs, as described in Section 2.2, K_{ini},
(2) application of the correction factor for fracture closure f attained after the previous iteration, i.e., $K_{ini} = f \cdot K_{ini}$ and correction by K_{grout}
(3) simulation of desaturation starting from hydrostatic conditions, to reach atmospheric pressure conditions, and
(4) simulation of resaturation and hydraulic tests.

Steps 3 and 4 are subdivided into time intervals, whose duration is automatically controlled by iTHOUGH2. At the end of each time interval, pressure values are examined, and fracture apertures recalculated according to Eq. (1) using the value of the closure rate α obtained after the previous iteration of the calibration procedure. Correspondingly, hydraulic conductivity varies with time. The closure law in Eq. (1) is not directly implemented in TOUGH2. Instead, a "stop-and-go" procedure is applied, i.e., iTOUGH2 is paused at the end of a time interval and the hydraulic conductivity field is updated externally. iTOUGH2 is then restarted to simulate the next time interval, using the updated hydraulic conductivity field and the pressure field at the end of the previous interval.

The extent and geometry of the EDZ after excavation is analysed in Geomechanica.[45] Six geomechanical simulations varying the stress tensor were carried out using a hybrid discrete-finite element method (Fig. 16) and are used here as training images depicting possible spatial patterns of the EDZ. These simulations are not calibrated against available stress and deformation measurements. As such, the initial extent and geometry of the EDZ is uncertain. In the same line of arguments, the initial state of

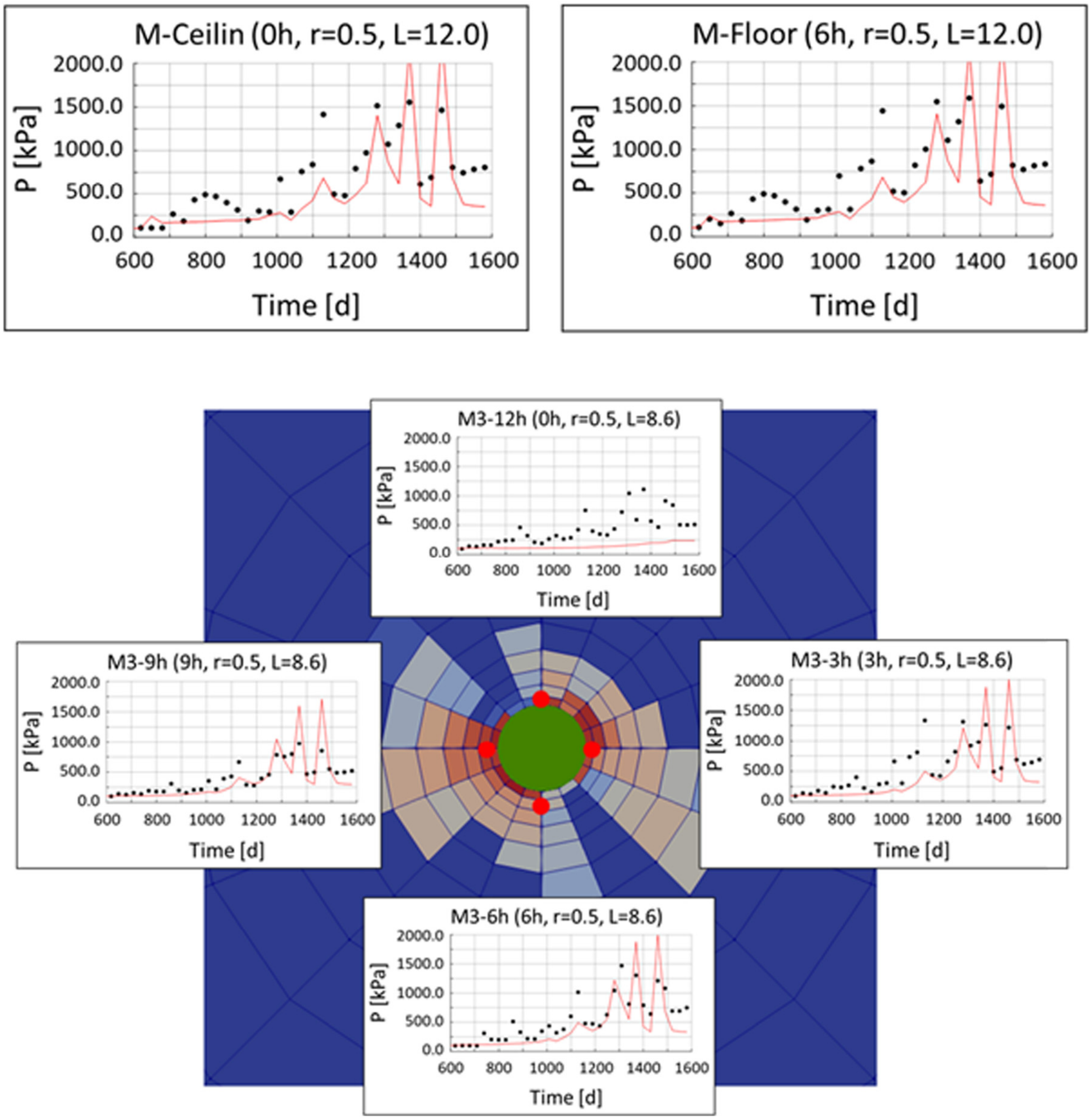

Fig. 18. Fits of measured pressures at selected sensors in the test (upper panels) and seal section, close to the test section (lower panel). In the insets, L and r denote length along the gallery axis (measured from the niche) and radial distance from the centre of the gallery.

resaturation is also highly uncertain. In addition, the longitudinal development of the EDZ is also uncertain. These problems are tackled by (1) testing different EDZ configurations by combining different training images along the gallery axis, and (2) calibrating the closure correction factor. The configuration presented here is summarized in Table 5.

3.2. Results

Several factors preclude the successful calibration of a large number of simulations. Amongst them, we highlight: (1) the high CPU usage (∼4800 s per direct run), (2) the anomalous behaviour of some pressure sensors and (3) the smearing of the boundary condition representing the multi-injection rate. Thus, this exercise aims at benchmarking and verifying the suggested methodology by providing realistic 3D simulations of the heterogeneity of the EDZ, in the sense of reproducing the trends monitored at available observation points, rather than at presenting a perfect fit of measurements that would lead to implausible EDZ representations.

The calibrated hydraulic conductivity field of one EDZ realization is displayed in Fig. 17. The goodness of fit at the test and seal sections is displayed in Fig. 18. As observed, the goodness of fit is satisfactory at sensors close to the rim of the gallery. The quality of the fit worsens with radial distances (Fig. 19). The model tends to overestimate pressure at radial distance $r > 1$ m. This is attributed to a combination of three factors, (1) the small extent and low significance of the EDZ, as represented in the training images and (2), the low values of calibrated parameters. The estimated closure correction factor ($f = 0.04$) reduces the hydraulic significance of the EDZ by almost two orders of magnitude. The estimated closure rate is $\alpha = -10.5$, very small compared to that in Ref. 6. Such value leads to very small fracture apertures, regardless of overpressure. The hydraulic conductivity of the grouted breakouts is also two orders of magnitude smaller than expected ($K_{grout} = 5{\cdot}10^{-17}$ m/s). These parameter values lead to an overall low conductive EDZ that yields a good fit of overpressures at sensors close to the gallery but precludes a good fit far from it.

The quality of the fits also degrades with distance from the boundary condition at the test section (Fig. 20). This highlights (1)

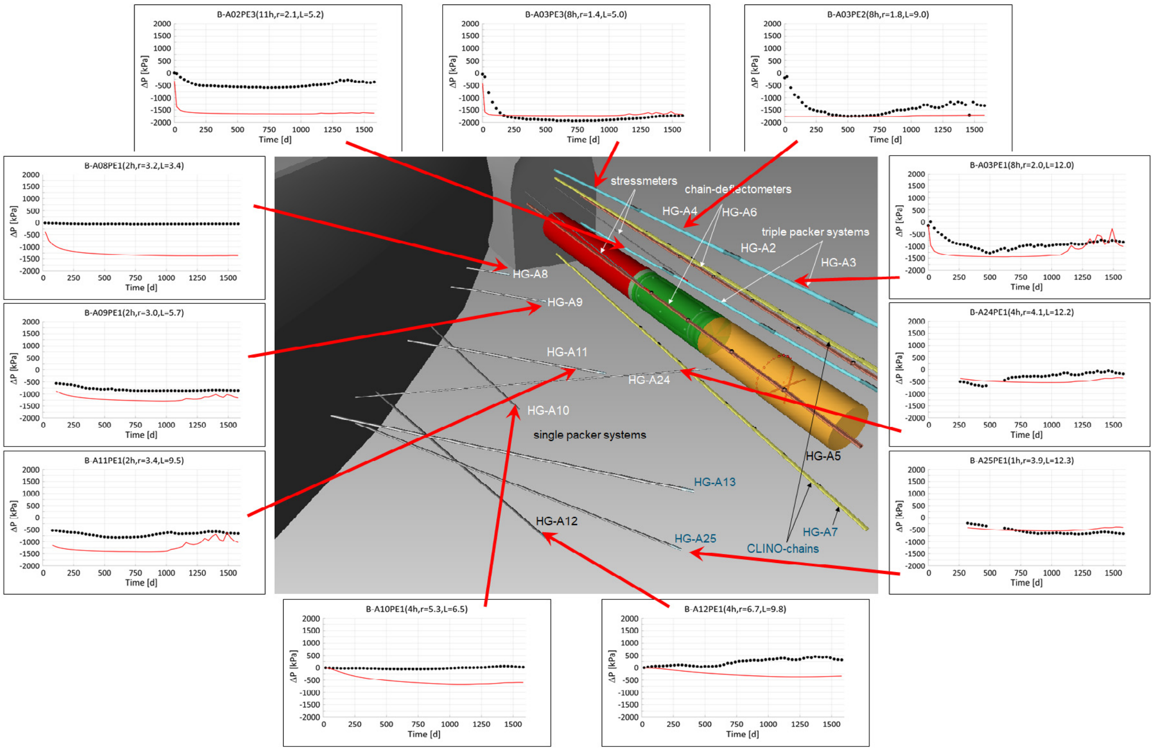

Fig. 19. Fits attained at different sensors along the gallery and at different radial distances. Circles depict measured pressures and the red line depicts calculated values. In the insets, L and r denote length along the gallery axis (from the end of the test section) and radial distance from the centre of the gallery.

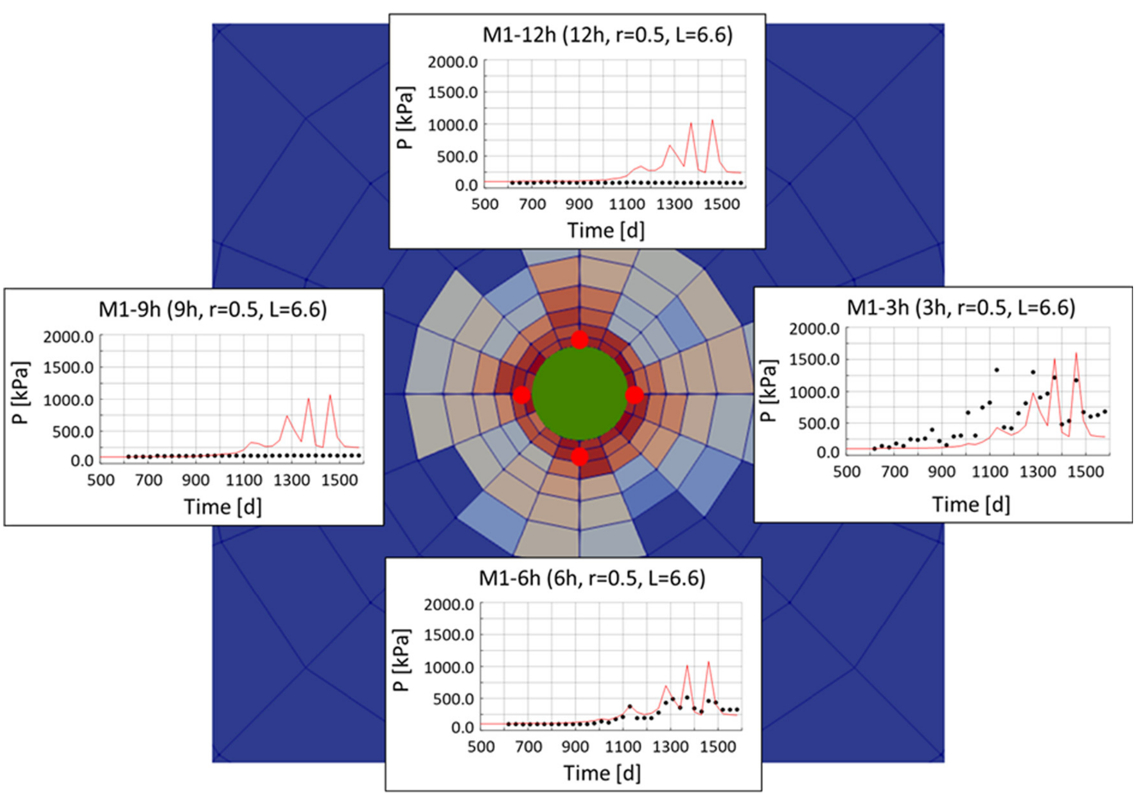

Fig. 20. Fits of measured pressures at selected sensors and seal section, close to the open section. In the insets, L and r denote length along the gallery axis (measured from the niche) and radial distance from the centre of the gallery.

the strong influence of the boundary condition and therefore the impact of the smearing in the calibration, (2) the large uncertainty on the development of the EDZ along the gallery axis and, (3) the influence of the initial hydromechanical response to excavation. As observed in Fig. 20, the model does not capture the observed variability (e.g., no overpressure in sensors M1-9h and M1-12h, but some response in M1-3h and M1-6h). This can be attributed to (1) grouted breakouts around the gallery not included in the model, (2) the presence of preferential flow paths around M1-9h and M1-12h, not captured by the model, or (3) some failure in the aforementioned sensors.

4. Conclusions

The Excavation Damage Zone (EDZ) around galleries and shafts of a deep geological repository for radioactive waste represents a viable release path for radionuclides and corrosion and degradation gases. As such, the EDZ needs to be addressed quantitatively in long-term probabilistic safety assessments. The EDZ is commonly represented by complex Discrete Fracture Network models that are not amenable to probabilistic (CPU costly) analyses. In addition, such models are most often 2D and therefore not capable of mimicking the naturally occurring three-dimensional physical phenomena. Previous work has been devoted to the generation of simplified 2D EDZ models with equivalent hydraulic behaviour.[6,36] This work presents an extension of the 2D methodology to generate stochastic 3D simulations of the EDZ.

The methodology relies on Marked Point Process techniques, according to which each fracture of the DFN is replaced by a representative point (i.e., its centroid) and a set of attributes defining its geometry (i.e., length, aperture and orientation). Such properties are scanned from a DFN mimicking the excavation process that serves as training image, and a set of 2D simulations of the EDZ are generated that inherit the geometric and statistical patterns of the original DFN. These 2D simulations are randomly stacked to render 3D continuum equivalent models of the EDZ. The methodology has been illustrated with the calibration of a multi-rate injection in the context of the HG-A experiment in Mont Terri (Switzerland). Results show a good fit of pressures measured at observation sensors near the excavated gallery and close to the boundary condition at the test section. Yet, the goodness of fit degrades far from these locations. This is attributed to: (1) the uncalibrated DFNs used as training images that lead to uncertainties on the original extent and hydraulic significance of the EDZ, (2) a smeared boundary condition representing the multi-rate injection, and (3) the uncertainty on the development of the EDZ parallel to the gallery axis.

Much remains to be done. The high CPU usage precluded the calibration of a large number of simulations. A parallel calibration scheme should be implemented to alleviate this problem. This would allow the evaluation of the uncertainties on the EDZ shape and extent along the direction parallel to the gallery axis. Yet, the fact that the global trends measured during a complex injection experiment are reproduced by the 3D model should be viewed as a step forward in the 3D stochastic modelling of the EDZ.

Acknowledgements

This work has been supported by the Swiss National Cooperative for the Disposal of Radioactive Waste (NAGRA; contract 13116) and the Mont Terri Consortium, representing the partners of the HG-A experiment ANDRA (France), BGR (Germany), NWMO (Canada), NAGRA and Swisstopo (Switzerland). The first author developed part of this work during his time with TK Consult AG.

References

1. Leupin OX, Smith P, Marschall P, Johnson L, Savage D, Cloet V, Schneider J, Senger R. High-level waste repository-induced effects. NAGRA Technical Report 14-13; 2016.
2. Tsang CF, Bernier F, Davies C. Geohydromechanical processes in the Excavation DamagedZone in crystalline rock, rock salt, and indurated and plastic clays in the context of radioactive waste disposal. *Int J Rock Mech Min Sci*. 2005;42:109–125.
3. Alheid HJ, Aranyossy JF, Blümling P, Hoteit N, Van Geet M. EDZ Development and Evolution –State of the Art. NF-PRO, Contract Number F16W-CT-2003-02389. European Commission, Luxembourg; 2007.
4. Tsang CF, Neretnieks I, Tsang Y. Hydrologic issues associated with nuclear waste repositories. *Water Resour Res*. 2015;51(9). http://dx.doi.org/10.1002/2015WR017641.
5. Jackson CP, Hoch AR, Todman S. Self-consistency of a heterogeneous continuum porousmedium representation of a fractured medium. *Water Resour Res*. 2000;36:189–202.
6. Alcolea A, Kuhlmann U, Marschall P, Lisjak A, Grasselli G, Mahabadi O, De La Vaissière RDe La, Leung H, Shao H. A pragmatic approach to abstract the excavation damaged zone around tunnels of a geological radioactive waste repository: application to the HG-A experiment in Mont Terri. *Geol Soc London, Spec Publ*. 2016;443. http://dx.doi.org/10.1144/SP443.8.
7. McNeish J. Total System Performance Assessment-License Application/ Methods and Approach. DOE, 2003; DOC.20031215-0001.
8. Sevougian SD, Jain V, Luik AV. The integration and abstraction of EBS models in Yucca Mountain Performance Assessment. Sandia Lab. Technical Report SAND2006-0172P 2006.
9. Lanyon GW, Senger R. A structured approach to the derivation of effective properties for combined water and gas flow in the EDZ. *Transp Porous Media*. 2011;90:95–112.
10. Hawkins IR, Swift BT, Hoch AR, Wendling J. Comparing flows to a tunnel for single porosity,double porosity and discrete fracture representations of the EDZ. *Phys Chem Earth*. 2011;36:1990–2002.
11. Bénet LV, Blaud E, Wendling J. Modelling of water and gas flow through an excavation damaged zone in the Callovo-Oxfordian argillites in the framework of a single porosity model. *Geol Soc London, Spec Publ*. 2016;443. http://dx.doi.org/10.1144/SP443.6.
12. An HM, Liu HY, Han H, Zheng X, Wang XG. Hybrid finite-discrete element modelling of dynamic fracture and resultant fragment casting and muck-piling by rock blast. *Comput Geotech*. 2017;81:322–345.
13. Fakhimi A, Lanari M. DEM–SPH simulation of rock blasting. *Comput Geotech*. 2014;55:158–164.
14. Kazerani T, Zhao J. Micromechanical parameters in bonded particle method formodelling of brittle material failure. *Int J Numer Anal Methods Geomech*. 2010;34(18):1877–1895.
15. Kazerani T. Effect of micromechanical parameters of microstructure on compressiveand tensile failure process of rock. *Int J Rock Mech Min Sci*. 2013;64:44–55.
16. Gao FQ, Stead D. The application of a modified Voronoi logic to brittle fracturemodelling at the laboratory and field scale. *Int J Rock Mech Min Sci*. 2014;68:1–14.
17. Scholtès L, Donzé FV. A DEM model for soft and hard rocks: role of grain interlockingon strength. *J Mech Phys Solids*. 2013;61(2):352–369.
18. Mahabadi O, Kaifosh P, Marschall P, Vietor T. Three-dimensional FDEM numerical simulation of failure processes observed in Opalinus Clay laboratory samples. *J Rock Mech Geot Eng*. 2014. http://dx.doi.org/10.1016/j.jrmge.2014.10.005.
19. Curran JH, Hammah RE. Keynote Lecture: Seven lessons of geomechanics software development. ARMA/USRMS 06-1012, 2006.
20. Hu LY, Chugunova T. Multiple-point geostatistics for modeling subsurface heterogeneity: A comprehensive review. *Water Resour Res*. 2008;44(11). http://dx.doi.org/10.1029/2008WR006993.
21. Mariethoz G, Caers J. *Multiple-Point Geostatistics: Stochastic Modeling with Training Images*. Ed. Wiley-Blackwell; 2014:376.
22. Strebelle S. Conditional simulation of complex geological structures using multiple-point statistics. *Math Geol*. 2002;34(1):1–21.
23. Mariethoz G, Renard P, Straubhaar J. The direct sampling method to perform multiple-point geostatistical simulations. *Water Resour Res*. 2010;46(11). http://dx.doi.org/10.1029/2008WR007621.
24. Alcolea A, Renard P. Blocking Moving Window algorithm: Conditioning multiple-point simulations to hydrogeological data. *Water Resour Res*. 2010;46. http://dx.doi.org/10.1029/2009WR007943.
25. Comunian A, Renard P, Straubhaar J. 3D multiple-point statistics simulation using 2D training images. *Comput Geosci*. 2012;40:49–65.
26. Berkowitz B. Analysis of fracture network connectivity using percolation theory. *Math Geol*. 1995;27(4):467–483.
27. Jacobsen M. *Point Process Theory and Applications: Marked Point and Piece- wise Deterministic Processes. Applied Probability and Statistics*. BirkhÃďuser; 2006.
28. Xu C, Dowd PA. A new computer code for discrete fracture network modelling. *Comput Geosci*. 2010;36:292–301.
29. Xu C, Dowd PA, Wyborn D. Optimisation of a stochastic rock fracture model using Markov Chain Monte Carlo simulation. *Mining Technology*. 2013;122(3):153–158.
30. Berrone S, Pieraccini S, Scialo S, Vicini F. A parallel solver for large scale DFN flow simulations. *SIAM J Sci Comput*. 2015;37(3):285–306.
31. Alghalandis YF, Xu C, Dowd PA. A general framework for fracture intersection analysis: algorithms and practical applications. In: *Proceedings of the 2011 Australian Geothermal Energy Conference*. 2011:15–20.

32. Geomechanica. Extent and shape of the EDZ around underground structures of a geological repository for radioactive waste –A sensitivity study for the candidate host rocks in the proposed siting regions in Northern Switzerland. NAGRA Technical Report NAB 13-78; 2013.
33. Ross S. *Introduction to Probability Models, 10th Edition*. Elsevier; 2010.
34. Cox DR, Isham VI. *Point Processes*. Chapman & Hall; 1980;.
35. Jong HM, Chen LG, Chiueh TD. Parallel Architecture for 3-Step Hierarchical Search Block-Matching Algorithm. *IEEE Trans Circuits Syst Video Technol.* 1994;4(4):407–416.
36. Alcolea A, Kuhlmann U, Lanyon GW, Marschall P. Hydraulic Conductance of the EDZ Around Underground Structures of a Geological Repository for Radioactive Waste –A SensitivityStudy for the Candidate Host Rocks in the Proposed Siting Regions in Northern Switzerland. NAGRA Technical Report NAB 13; 2014.
37. Lanyon GW, Martin D, Giger S, Marschall P. Development and evolution of the Excavation Damaged Zone (EDZ) in the Opalinus Clay –A synopsis of the state of knowledge from Mont Terri. Nagra Arbeitsbericht NAB 14-87; 2014.
38. Meier P, Trick Th, Blümling P, Volckaert G. Self-healing of fractures at the Mont Terri Rock Laboratory: results after one year of experimental work. In: *Proceedings of International Workshop on Geomechanics, Hydromechanical and Thermohydro-mechanical Behavior od Deep Argilaceous Rocks: Theory and experiments*. 2000, Paris.
39. Martin CC, Lanyon GW, Bossart P, Blümling P. Excavation Disturbed Zone (EDZ) in Clay Shale: Mont Terri. Mont Terri Technical Report TR 2001-01, 2004.
40. Harrington J, Volckaert G, Jacobs E, Maes N, Areias L, Charlier R, Frédéric C, Gerard P, Radu JP, Svoboda J, Granet S, Alcoverro J, Arnedo D, Olivella S, Alonso E, Marschall P, Gaus I, Rüedi J, Cuss R, Sathar S, Noy D. Summary report: Experiments and modelling of excavation damage zone (EDZ) behaviour in argillaceous and crystalline rocks (Work Package 4); EC FORGE Project Report D4.24-R; 2013.
41. Marschall P, Giger S, De La Vassière S, Shao H, Leung H, Nussbaum C, Trick T, Lanyon B, Senger R, Lisjak A, Alcolea A. Hydro-mechanical evolution of the EDZ as a transport path for radionuclides and gas: insights from a dedicated experimental programme in the Mont Terri URL. *Swiss J Geosci*. 2017;110:173–194. http://dx.doi.org/10.1007/s00015-016-0246-z.
42. Nagra. Projekt Opalinuston –Synthese der geowissenschaftlichen Untersuchungs-ergebnisse. Entsorgungsnachweis für abgebrannte Brennelemente, verglaste hochaktive sowie langlebige mittelaktive Abfälle. Nagra Technical Report NTB 02-03; 2002.
43. Alcolea A, Kuhlmann U, Lanyon GW, Marschall P. Hydraulic conductance of the EDZ around underground structures of a geological repository for radioactive waste –Application to the HG-A experiment in Mont Terri NAGRA Technical Report NAB 15-42; 2015.
44. Lanyon GW, Marschall P, Trick T, de la Vaissiere R, Shao H, Leung H. Self-sealing experiments and gas injection tests in a backfilled microtunnel of the Mont Terri URL. *Geol Soc London, Spec Publ*. 2014;400(1):93–106. http://dx.doi.org/10.1144/SP400.8.
45. Geomechanica. HGA experiment: numerical simulation of the EDZ formation and mechanical re-compaction process using a FDEM approach. Mont Terri Project Technical Note TN 2014-89, 2014.
46. Marschall P, Distinguin M, Shao H, Bossart P, Enachescu C, Trick Th. Creation and evolution of damage zones around a microtunnel in a claystone formation of the Swiss Jura Mountains. In: *SPE International Symposium and Exhibition on Formation Damage Control*. Richardson, Texas: Society of Petroleum Engineers; 2006*SPE Paper 98537*.
47. Lanyon GW, Marschall P, Trick T, de la Vaissière R, Shao H, Leung H. Hydromechanical Evolution and self-sealing of damage zones around a microtunnel in a claystone formation of the Swiss Jura mountains. In: *43rd US Rock Mechanics Symposium and 4th US - Canada Rock Mechanics Symposium*. 2009:652–663.
48. Finsterle S. iTOUGH2 User's Guide. Lawrence Berkeley National Laboratory Technical Report LBNL-40040; 2007.
49. Finsterle S. iTOUGH2 Universal Optimization Using the PEST Protocol —User's Guide. Lawrence Berkeley National Laboratory Technical Report LBNL-3698E; 2010.
50. Marschall P, Trick Th, Lanyon GW, Delay J, Shao H. Hydro-mechanical evolution of damaged zones around a microtunnel in a claystone formation of the swiss jura mountains. In: *Proceedings of the 42nd U.S. Rock Mechanics Symposium (USRMS)*, San Francisco 2008, ARMA-08-193.
51. Yong S, Kaiser PK, Loew S. Influence of tectonic shears on tunnel-induced fracturing. *Int J Rock Mech Min Sci*. 2010;47:894–907.
52. Fine RA, Millero FJ. Compressibility of water as a function of temperature and pressure. *J Chem Phys*. 1973;59(10):5529.
53. Poppei J, Mayer G, Croisé J, Marschall, P. Modelling of resaturation, gas migration and thermal effects in a SF/ILW repository in low-permeability overconsolidated clay-shale. In: *Proceedings of TOUGH Symposium*. 2003, Berkeley.